9-2012

The Chandra X-Ray Point-Source Catalog in The Deep2 Galaxy Redshift Survey Fields

A. D. Goulding
Harvard-Smithsonian Center for Astrophysics

W. R. Forman
Harvard-Smithsonian Center for Astrophysics

R. C. Hickox
Dartmouth College

C. Jones
Harvard-Smithsonian Center for Astrophysics

THE *CHANDRA* X-RAY POINT-SOURCE CATALOG IN THE DEEP2 GALAXY REDSHIFT SURVEY FIELDS

A. D. Goulding[1], W. R. Forman[1], R. C. Hickox[1,2,3], C. Jones[1], R. Kraft[1], S. S. Murray[1,4], A. Vikhlinin[1],
A. L. Coil[5], M. C. Cooper[6,†], M. Davis[7], J. A. Newman[8]

Draft version April 24, 2018

ABSTRACT

We present the X-ray point-source catalog produced from the *Chandra* Advanced CCD Imaging Spectrometer (ACIS-I) observations of the combined ~ 3.2 deg^2 DEEP2 (XDEEP2) survey fields, which consist of four ~ 0.7–1.1 deg^2 fields. The combined total exposures across all four XDEEP2 fields range from ~ 10ks–1.1Ms. We detect X-ray point-sources in both the individual ACIS-I observations and the overlapping regions in the merged (stacked) images. We find a total of 2976 unique X-ray sources within the survey area with an expected false-source contamination of ≈ 30 sources ($\lesssim 1\%$). We present the combined log N – log S distribution of sources detected across the XDEEP2 survey fields and find good agreement with the Extended *Chandra* Deep Field and *Chandra*-COSMOS fields to $f_{\rm X,0.5-2keV} \sim 2 \times 10^{-16}$ erg cm^{-2} s^{-1}. Given the large survey area of XDEEP2, we additionally place relatively strong constraints on the log N – log S distribution at high fluxes ($f_{\rm X,0.5-2keV} \sim 3 \times 10^{-14}$ erg cm^{-2} s^{-1}), and find a small systematic offset (a factor ~ 1.5) towards lower source numbers in this regime, when compared to smaller area surveys. The number counts observed in XDEEP2 are in close agreement with those predicted by X-ray background synthesis models. Additionally, we present a Bayesian-style method for associating the X-ray sources with optical photometric counterparts in the DEEP2 catalog (complete to $R_{\rm AB} < 25.2$) and find that 2126 ($\approx 71.4 \pm 2.8\%$) of the 2976 X-ray sources presented here have a secure optical counterpart with a $\lesssim 6\%$ contamination fraction. We provide the DEEP2 optical source properties (e.g., magnitude, redshift) as part of the X-ray–optical counterpart catalog.

Subject headings: galaxies: active – surveys – X-rays: galaxies

1. INTRODUCTION

Understanding the role of active galactic nuclei (AGN) in galaxy evolution is a major focus in present day astrophysics. It is now becoming increasingly clear that, despite their vastly differing size-scales, the evolution of massive host galaxies and the growth of their central supermassive black holes (SMBHs) may not be independent events (e.g., Boyle & Terlevich 1998; Hopkins et al. 2006; Silverman et al. 2009; Hopkins et al. 2008; Smolčić et al. 2009). Indeed, AGN activity and galaxy properties, such as luminosity, color and morphology, are shown to evolve with time. The redshift range $z \sim 1$–2 is a crucial epoch: (1) galaxies are evolving strongly as a function of stellar mass (e.g., Zheng et al. 2009; Franceschini et al. 1999; Serjeant et al. 2010); (2) AGN activity is prevalent

E-mail:- agoulding@cfa.harvard.edu
[1] Harvard-Smithsonian Center for Astrophysics, 60 Garden St., Cambridge, MA 02138, USA
[2] Department of Physics and Astronomy, Dartmouth College, Hanover, NH 03755, USA
[3] Department of Physics, University of Durham, South Road, Durham DH1 3LE, UK
[4] Department of Physics and Astronomy, Johns Hopkins University, 3400 North Charles Street, Baltimore, MD 21218, USA
[5] Department of Physics, Center for Astrophysics and Space Sciences, University of California at San Diego, 9500 Gilman Dr., La Jolla, San Diego, CA 92093
[6] Center for Galaxy Evolution, Department of Physics and Astronomy, University of California, Irvine, 4129 Frederick Reines Hall, Irvine, CA 92697, USA
[†] Hubble Fellow
[7] Department of Astronomy, University of California, Berkeley, Hearst Field Annex B, Berkeley, CA 94720, USA
[8] Department of Physics and Astronomy, University of Pittsburgh, 3941 O'Hara Street, Pittsburgh, PA 15260, USA

(e.g., Ueda et al. 2003; Hasinger et al. 2005; La Franca et al. 2005; Barger et al. 2005; Richards et al. 2006); (3) massive clusters are forming (e.g., Lidman et al. 2008; Hilton et al. 2009; Papovich et al. 2010; Fassbender et al. 2011; Bauer et al. 2011; Mehrtens et al. 2012; Nastasi et al. 2011) and (4) the red sequence is becoming established (e.g., Bell et al. 2004; Faber et al. 2007; Willmer et al. 2006; Brand et al. 2005; Domínguez Sánchez et al. 2011). To unambiguously determine the dominant physical processes that are driving the growth and evolution of galaxies and their central black holes requires sensitive, wide-field spectroscopic surveys of AGN.

Sensitive blank-field X-ray surveys arguably provide the most efficient selection of AGN that is unbiased to moderate-to-high obscuration, and in general is not readily contaminated by host-galaxy emission. Indeed, as star-formation is relatively weak at X-ray energies ($L_{\rm X,0.5-8keV} \lesssim 10^{42}$ erg s^{-1}; Moran et al. 1999; Lira et al. 2002), selection of AGN at these wavelengths can identify many of the most low-luminosity and/or obscured systems (e.g., Fukazawa et al. 2001; Done et al. 1996; Risaliti et al. 1999; Matt et al. 1996; Maiolino et al. 1998; Georgantopoulos et al. 2009). By harnessing the unprecedented angular resolution provided by the *Chandra* X-ray Observatory, both deep and wide-field X-ray surveys have been instrumental in our current understanding of AGN evolution (e.g., Kenter et al. 2005; Nandra et al. 2005; Worsley et al. 2005; Brandt & Hasinger 2005; Brand et al. 2006; Hasinger et al. 2007; Laird et al. 2009). To date, the two deepest X-ray surveys are the pencil-beam (~ 0.1 deg^2) ~ 4 Ms *Chandra* Deep Field South (CDF-S; Giacconi et al. 2002; Luo et al. 2008;

Xue et al. 2011) and the ~ 2 Ms *Chandra* Deep Field North (CDF-N; Alexander et al. 2003b) which have successfully identified AGN across more than 95% of cosmic time (out to $z \sim 7$). Complementary to the highest redshift sources detected in the deep fields, nearby ($z < 0.8$) AGN, identified in the relatively shallow contiguous wide-field surveys, such as the 5 ks ~ 9.3 deg^2 XBootes field (Murray et al. 2005; Kenter et al. 2005; Brand et al. 2006), have provided the ability to measure *environment*, a key component in galaxy and AGN evolution (e.g., Cooper et al. 2005, 2006; Georgakakis et al. 2008; Coil et al. 2009; Hickox et al. 2009; Cappelluti et al. 2010; Gilli et al. 2009). Furthermore, these wide-field X-ray surveys serendipitously detect significant numbers of rare, extremely luminous AGN and dozens of extended groups and clusters, which allow for a more complete understanding of the most massive SMBHs and cosmic structures in the Universe.

However, the peak of AGN activity, both in total luminosity and relative abundance is believed to occur at $z \sim 1$–2 (e.g., Hopkins et al. 2007; Zheng et al. 2009; Serjeant et al. 2010). The 3.6 deg^2 DEEP2 Galaxy Redshift Survey (Davis et al. 2003; Madgwick et al. 2003) provides one of the most detailed censuses of the $z \sim 1$ Universe. DEEP2 is currently one of the widest area and most complete spectroscopic surveys of $z > 1$ galaxies, making it the ideal survey to target large numbers of AGN at $z \sim 1$–2. Indeed, the fourth data release (DR4) of the survey contains spectra for $\sim 50,300$ distant galaxies (with $R_{AB} < 24.1$) within four ~ 0.7–1.1 deg^2 fields, which are primarily in the redshift range $z \sim 0.75$–1.4; these were collected using the DEIMOS spectrograph ($R \sim 5000$ in the wavelength range $6400 < \lambda < 9200$Å) on the Keck II telescope. A complete description of the DEEP2 DR4 spectroscopic catalog is available in Newman et al. (2012).

We have used the *Chandra* Advanced CCD Imaging Spectrometer (ACIS-I) to provide high-angular resolution X-ray coverage across almost the entire ~ 3.6 deg^2 survey area covered by the four DEEP2 fields (Field 1 - PI:K.Nandra; Fields 2, 3 and 4 - PI:S.Murray). Here we present the X-ray source catalog for our *Chandra* ACIS-I observations of the combined ~ 3.2 deg^2 DEEP2 (XDEEP2) survey. The four contiguous XDEEP2 fields have combined total exposures ranging from ~ 10ks – 1Ms. In section 2 we present a brief introduction to the construction of the survey fields and the data reduction and processing of the X-ray observations. In section 3 we provide an in-depth methodology for the detection of the point sources and the building of the final XDEEP2 catalog. In section 4, we compare our new catalog of Field 1 (the Extended Groth strip), which now includes three recent ~ 600 ks ACIS-I observations, to the previous catalog of Laird et al. (2009), and compare the XDEEP2 catalog to the *Chandra* Source Catalog (Evans et al. 2010). We further present the flux band ratio and density of number count distributions for the XDEEP2 catalog. In section 5, we outline the optical–X-ray source matching technique used to compare our new X-ray catalog with the Fourth Data Release of the optical DEEP2 photometric catalog. Finally, in section 6 we present a summary of our findings. Throughout the manuscript we adopt a standard flat ΛCDM cosmology

with $H_0 = 71$ km s^{-1} Mpc^{-1} and $\Omega_M = 0.3$.

When combined, the redshift and galaxy property information established using the DEEP2 optical spectra and the AGN identified using the new *Chandra* X-ray observations provide one of the most complete views of AGN activity and the growth of large scale structure at $z \sim 1$–2. In forthcoming papers we will present a statistically complete and obscuration-independent view of the evolution of AGN and their host-galaxies identified across the entire electromagnetic spectrum, in the epoch $z \sim 1.5$ to the present-day.

2. *CHANDRA* X-RAY OBSERVATIONS

2.1. *Construction of the XDEEP2 fields*

The XDEEP2 survey region consists of four contiguous ~ 0.7–1.1 deg^2 fields covered by *Chandra* ACIS-I observations. The field positions, arrangements and main properties are outlined in Table 1. The total area covered by XDEEP2 is ≈ 3.2 deg^2. X-ray catalogs for the previous 200 ks observations in Field 1, also referred to as the Extended Groth Strip, have been presented in Nandra et al. (2005) and Laird et al. (2009). For consistency and ease of reference to the previous Field 1 catalogs, we adopt the same sub-field naming convention defined in Laird et al. (2009) (see column 2 of Table 2). Additionally, in this manuscript we include the more recent 600 ks ACIS-I observations within three sub-fields (EGS-3; EGS-4; EGS-5) of the Groth Strip centered at $\alpha = 215.0733^o$, $\delta = +53.008^o$; 214.808^o, $+52.806^o$; 214.527^o, $+52.622^o$, which for distinction between this and the previous catalogs, we rename as AEGIS-1, AEGIS-2 and AEGIS-3, respectively.

The catalog presented here was derived from multi-
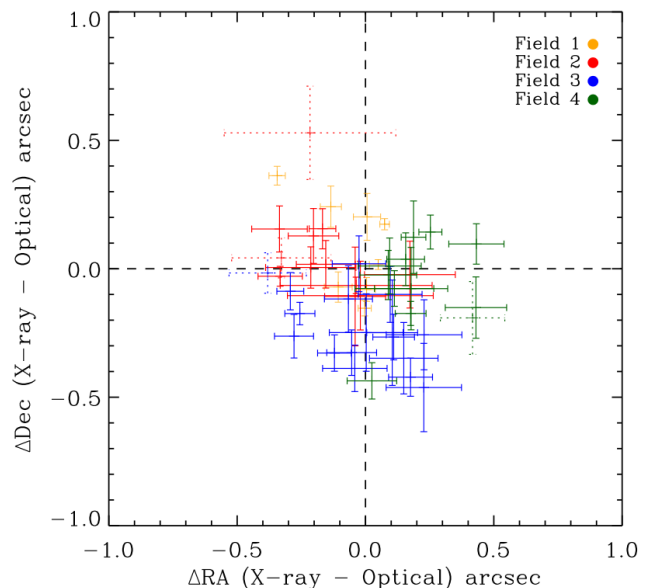
FIG. 1.— Median offsets between optical and X-ray source positions with associated rms uncertainties in arc-seconds are plotted for the eight merged sub-fields in XDEEP2 Field 1 and the individual ObsIDs for Fields 2, 3 and 4. These median offsets were used to calculate astrometric corrections for the sub-fields in Field 1 and the individual X-ray observations in Fields 2–4. *Chandra* ObsIDs containing five or fewer X-ray–optical counterparts within 5 arc-minutes of the observation aim-point are shown with dotted error bars.

TABLE 1
XDEEP2 FIELD PROPERTIES

Field #[a]	Pointings[b]	α_{center}[c]	δ_{center}[c]	Total Area[d]	$\text{Exp}_{\text{Eff},20\%}$[e]	$\text{Exp}_{\text{Eff},80\%}$[f]
		(deg)	(deg)	(deg^2)	(ks)	(ks)
1	96	214.7388	+52.7838	0.66	662.3	139.2
2	12	252.4470	+34.9300	0.74	15.8	8.1
3	17	352.4711	+0.1869	1.13	10.1	8.1
4	12	37.2497	+0.5916	0.75	15.9	8.2

[a]XDEEP2 field number
[b]Number of *Chandra* pointings within field
[c]Center co-ordinates of field in degrees as projected onto the sky in J2000 system
[d]Total projected area of field in square degrees
[e]Effective exposure in kilo-seconds at 20% of total field area
[f]Effective exposure in kilo-seconds at 80% of total field area

epoch observations taken during AO3 (PI K. Nandra), AO6 and AO9, combined with Guaranteed Time Observations (PI S. Murray; AO9). All *Chandra* observations for XDEEP2 are publicly available through the *Chandra* X-ray Center Archive. XDEEP2 consists of 126 separate pointings with varying individual exposures ($\sim$ 3–85 ks).

With the exception of three exposures, all XDEEP2 observations were performed in VFAINT mode to allow for the best possible background rejection. ObsIDs 3305, 4537 and 4365 were taken in FAINT mode. In Table 2 we provide the individual pointing details for each observation and field.

TABLE 2 Observation Log.

Field[a]	ObsID[b,c]	Sub-field[d]	Obs. Start[e]	Exp[f]	α_{J2000}[g]	δ_{J2000}[g]	Roll[h]	Mode[i]
			(UT)	(ks)	(deg)	(deg)	(deg)	
1	3305	EGS-8	2002-08-11 21:43:57	29.40	214.42932	52.47367	84.74	FAINT
1	4357	EGS-8	2002-08-12 22:32:00	84.36	214.42932	52.47367	84.74	FAINT
1	4365	EGS-8	2002-08-21 10:56:53	83.75	214.42933	52.47367	84.74	FAINT
1	5841	EGS-1	2005-03-14 00:04:09	44.45	215.67386	53.43149	229.11	VFAINT
1	5842	EGS-1	2005-03-16 15:54:34	46.42	215.67348	53.43141	226.09	VFAINT
1	5843	EGS-2	2005-03-19 17:13:09	44.46	215.38301	53.22857	222.38	VFAINT
1	5844	EGS-2	2005-03-21 22:37:40	45.85	215.38274	53.22848	219.86	VFAINT
1	5845	AEGIS-1 (EGS-3)	2005-03-24 14:33:31	48.40	215.11277	53.03769	216.61	VFAINT
1	5846	AEGIS-1 (EGS-3)	2005-03-27 04:51:15	49.40	215.11244	53.03755	213.67	VFAINT
1	5847	AEGIS-2 (EGS-4)	2005-04-06 20:01:09	44.55	214.84408	52.84563	200.99	VFAINT
1	5848	AEGIS-2 (EGS-4)	2005-04-07 21:03:59	44.45	214.84409	52.84563	200.99	VFAINT
1	5849	AEGIS-3 (EGS-5)	2005-10-11 12:47:43	49.46	214.59049	52.64737	19.89	VFAINT
1	5850	AEGIS-3 (EGS-5)	2005-10-14 05:15:37	45.55	214.59075	52.64755	16.94	VFAINT
1	5851	EGS-6	2005-10-15 03:03:18	35.68	214.10808	52.33121	14.80	VFAINT
1	5852	EGS-6	2005-12-03 13:00:33	10.62	214.10950	52.33506	324.80	VFAINT
1	5853	EGS-7	2005-10-16 20:16:24	42.57	213.84975	52.13788	14.04	VFAINT
1	5854	EGS-7	2005-09-30 23:52:23	50.07	213.84816	52.13692	31.03	VFAINT
1	6210	EGS-1	2005-10-03 14:56:50	45.94	215.68094	53.42341	29.70	VFAINT
1	6211	EGS-1	2005-10-12 11:43:28	35.64	215.68196	53.42394	19.80	VFAINT
1	6212	EGS-2	2005-10-04 22:56:06	46.28	215.39109	53.22076	28.00	VFAINT
1	6213	EGS-2	2005-10-06 06:52:13	47.51	215.39126	53.22084	26.47	VFAINT
1	6214	AEGIS-1 (EGS-3)	2005-09-28 08:09:03	47.50	215.12071	53.02977	35.13	VFAINT
1	6215	AEGIS-1 (EGS-3)	2005-09-29 15:58:09	48.63	215.12088	53.02982	33.67	VFAINT
1	6216	AEGIS-2 (EGS-4)	2005-09-20 09:35:13	49.48	214.85259	52.83816	43.79	VFAINT
1	6217	AEGIS-2 (EGS-4)	2005-09-23 01:34:59	49.50	214.85259	52.83816	43.79	VFAINT
1	6218	AEGIS-3 (EGS-5)	2005-10-07 05:31:36	40.58	214.59005	52.64709	24.71	VFAINT
1	6219	AEGIS-3 (EGS-5)	2005-09-25 15:57:04	49.48	214.58864	52.64648	37.70	VFAINT
1	6220	EGS-6	2005-09-13 09:17:01	37.63	214.10431	52.32963	49.79	VFAINT
1	6222	EGS-7	2005-08-28 17:20:24	34.69	213.84478	52.13607	59.04	VFAINT
1	6223	EGS-7	2005-08-31 05:06:47	49.51	213.84477	52.13608	59.04	VFAINT
1	6366	EGS-7	2005-09-03 06:30:11	14.58	213.84476	52.13605	59.04	VFAINT
1	6391	EGS-6	2005-09-16 20:43:01	8.45	214.10440	52.32956	49.79	VFAINT
1	7169	EGS-6	2005-12-06 02:29:46	16.03	214.10951	52.33509	324.25	VFAINT
1	7180	EGS-1	2005-10-13 05:16:04	20.43	215.68191	53.42394	19.80	VFAINT
1	7181	EGS-6	2005-10-15 21:17:21	15.98	214.10803	52.33122	14.80	VFAINT
1	7187	EGS-7	2005-10-17 19:07:08	6.59	213.84962	52.13785	14.04	VFAINT
1	7188	EGS-6	2005-12-05 04:50:40	2.58	214.10909	52.33499	324.80	VFAINT
1	7236	EGS-6	2005-11-30 19:29:34	20.37	214.10952	52.33505	324.80	VFAINT
1	7237	EGS-6	2005-12-04 05:26:20	16.93	214.10947	52.33504	324.80	VFAINT
1	7238	EGS-6	2005-12-03 10:02:10	9.53	214.10956	52.33502	324.80	VFAINT
1	7239	EGS-6	2005-12-11 08:31:06	16.03	214.10932	52.33545	319.59	VFAINT
1	9450	AEGIS-1	2007-12-11 04:24:07	28.78	215.07183	53.00951	319.80	VFAINT
1	9451	AEGIS-1	2007-12-16 10:52:06	25.21	215.07180	53.00951	319.80	VFAINT
1	9452	AEGIS-1	2007-12-18 05:45:49	13.29	215.07001	53.01006	311.30	VFAINT
1	9453	AEGIS-1	2008-06-15 21:28:03	44.69	215.05924	52.99529	130.79	VFAINT
1	9454	AEGIS-2	2008-09-11 04:47:10	59.35	214.81134	52.80632	49.30	VFAINT
1	9455	AEGIS-2	2008-09-13 19:38:46	99.72	214.81134	52.80633	49.30	VFAINT
1	9456	AEGIS-2	2008-09-24 08:15:30	58.35	214.81276	52.80818	34.80	VFAINT

Continued on next page...

TABLE 2 – continued from previous page

Field	ObsID	Sub-field (UT)	Obs. Start (UT) (ks)	Exp (ks) (deg)	α_{J2000} (deg)	δ_{J2000} (deg)	Roll Angle	Mode
1	9457	AEGIS-2	2008-06-27 07:08:38	32.74	214.79607	52.80288	124.29	VFAINT
1	9458	AEGIS-3	2009-03-18 12:20:16	6.65	214.52536	52.62140	223.14	VFAINT
1	9459	AEGIS-3	2008-09-30 19:20:28	69.55	214.55046	52.61607	30.30	VFAINT
1	9460	AEGIS-3	2008-10-10 06:17:49	21.36	214.55050	52.61613	29.80	VFAINT
1	9461	AEGIS-3	2009-06-26 09:30:12	23.73	214.53241	52.61042	129.79	VFAINT
1	9720	AEGIS-1	2008-06-17 05:14:02	27.79	215.05922	52.99527	130.79	VFAINT
1	9721	AEGIS-1	2008-06-12 08:09:14	16.55	215.05741	52.99587	139.79	VFAINT
1	9722	AEGIS-1	2008-06-13 07:02:28	19.89	215.05735	52.99589	139.79	VFAINT
1	9723	AEGIS-1	2008-06-18 13:42:40	34.47	215.05923	52.99528	130.79	VFAINT
1	9724	AEGIS-1	2007-12-22 13:37:26	14.08	215.07007	53.01006	311.30	VFAINT
1	9725	AEGIS-1	2008-03-31 05:21:42	31.13	215.05145	53.00445	209.78	VFAINT
1	9726	AEGIS-1	2008-06-05 08:45:04	39.62	215.05737	52.99587	139.79	VFAINT
1	9727	AEGIS-2	2008-09-12 16:44:12	34.94	214.81132	52.80634	49.30	VFAINT
1	9729	AEGIS-2	2008-07-09 16:47:58	48.09	214.79710	52.80272	119.79	VFAINT
1	9730	AEGIS-2	2008-09-25 16:50:54	53.72	214.81277	52.80817	34.80	VFAINT
1	9731	AEGIS-2	2008-07-03 10:58:47	21.38	214.79688	52.80275	120.79	VFAINT
1	9733	AEGIS-2	2008-09-27 01:15:33	58.36	214.81275	52.80818	34.80	VFAINT
1	9734	AEGIS-3	2008-09-16 11:01:21	49.47	214.54931	52.61415	44.80	VFAINT
1	9735	AEGIS-3	2008-09-19 03:14:15	49.47	214.54930	52.61415	44.80	VFAINT
1	9736	AEGIS-3	2008-09-20 11:07:10	49.48	214.54930	52.61416	44.80	VFAINT
1	9737	AEGIS-3	2008-09-21 17:53:00	49.48	214.54931	52.61415	44.80	VFAINT
1	9738	AEGIS-3	2008-10-02 06:56:22	61.39	214.55047	52.61607	30.30	VFAINT
1	9739	AEGIS-3	2008-10-05 11:28:12	42.59	214.55049	52.61614	29.80	VFAINT
1	9740	AEGIS-3	2009-03-09 22:24:18	20.37	214.52625	52.62221	229.78	VFAINT
1	9793	AEGIS-1	2007-12-19 02:53:51	23.83	215.07005	53.01008	311.30	VFAINT
1	9794	AEGIS-1	2007-12-20 04:27:59	10.03	215.07009	53.01004	311.30	VFAINT
1	9795	AEGIS-1	2007-12-20 21:36:20	8.91	215.07008	53.01009	311.30	VFAINT
1	9796	AEGIS-1	2007-12-21 20:28:33	16.33	215.07004	53.01008	311.30	VFAINT
1	9797	AEGIS-1	2007-12-23 13:12:28	12.60	215.07007	53.01011	311.30	VFAINT
1	9842	AEGIS-1	2008-04-02 21:01:59	30.44	215.05145	53.00445	209.78	VFAINT
1	9843	AEGIS-1	2008-04-02 01:11:09	13.48	215.05143	53.00448	209.78	VFAINT
1	9844	AEGIS-1	2008-04-05 13:07:54	19.78	215.05147	53.00443	209.78	VFAINT
1	9863	AEGIS-1	2008-06-07 00:33:47	22.01	215.05733	52.99587	139.79	VFAINT
1	9866	AEGIS-1	2008-06-03 22:43:14	25.83	215.05737	52.99588	139.79	VFAINT
1	9870	AEGIS-1	2008-06-10 15:11:23	11.00	215.05736	52.99583	139.79	VFAINT
1	9873	AEGIS-1	2008-06-11 14:22:06	30.75	215.05737	52.99588	139.79	VFAINT
1	9875	AEGIS-1	2008-06-23 22:54:14	25.20	215.05968	52.99517	128.77	VFAINT
1	9878	AEGIS-2	2008-06-28 06:03:20	15.73	214.79613	52.80289	124.29	VFAINT
1	9879	AEGIS-2	2008-06-29 03:39:20	26.80	214.79612	52.80288	124.29	VFAINT
1	9880	AEGIS-2	2008-07-05 17:00:17	29.50	214.79688	52.80274	120.79	VFAINT
1	10769	AEGIS-3	2009-03-20 13:38:26	26.68	214.52497	52.62063	216.98	VFAINT
1	10847	AEGIS-3	2008-12-31 05:06:27	19.27	214.54102	52.62566	302.79	VFAINT
1	10848	AEGIS-3	2009-01-01 17:11:57	17.91	214.54109	52.62567	302.79	VFAINT
1	10849	AEGIS-3	2009-01-02 21:25:57	15.92	214.54106	52.62570	302.79	VFAINT
1	10876	AEGIS-3	2009-03-11 01:37:20	17.21	214.52626	52.62222	229.78	VFAINT
1	10877	AEGIS-3	2009-03-12 15:15:57	16.22	214.52630	52.62223	229.78	VFAINT
1	10896	AEGIS-3	2009-06-15 18:46:14	23.29	214.53123	52.61075	135.32	VFAINT
1	10923	AEGIS-3	2009-06-22 07:38:22	11.62	214.53239	52.61039	129.79	VFAINT
2	8631	-	2007-11-26 00:59:04	8.87	253.14712	35.06573	10.90	VFAINT
2	8632	-	2007-11-26 03:52:42	8.60	252.85635	35.06034	10.90	VFAINT
2	8633	-	2007-11-26 06:30:13	8.60	253.14626	34.84466	10.90	VFAINT
2	8634	-	2007-11-26 09:07:44	8.60	252.57252	35.05619	10.90	VFAINT
2	8635	-	2007-11-26 11:45:15	8.60	252.29343	35.04576	10.90	VFAINT
2	8636	-	2007-11-26 14:22:46	8.60	252.00739	35.04026	10.90	VFAINT
2	8637	-	2007-11-26 17:00:17	8.60	251.71914	35.03216	10.90	VFAINT
2	8638	-	2007-11-26 19:37:58	8.60	252.86086	34.84118	10.90	VFAINT
2	8639	-	2007-11-26 22:15:40	8.60	252.57546	34.83892	10.90	VFAINT
2	8640	-	2007-11-27 00:53:12	8.61	252.29954	34.82097	10.90	VFAINT
2	8641	-	2007-11-28 05:53:06	8.92	252.01425	34.81738	10.90	VFAINT
2	8642	-	2007-11-28 08:41:27	8.66	251.72431	34.81683	10.90	VFAINT
3	8601	-	2008-08-05 04:20:00	9.06	353.25281	0.24568	242.49	VFAINT
3	8602	-	2008-08-05 07:12:25	8.93	352.66172	0.28185	242.49	VFAINT
3	8603	-	2008-08-05 09:48:46	8.84	353.46809	0.20782	242.49	VFAINT
3	8604	-	2008-08-05 12:24:02	8.84	351.64001	0.25772	242.49	VFAINT
3	8605	-	2008-08-05 14:59:49	8.84	353.37170	0.01529	242.49	VFAINT
3	8606	-	2008-08-05 17:35:02	8.83	352.97330	0.21938	242.49	VFAINT
3	8607	-	2008-08-05 20:09:51	8.83	351.89874	0.25007	242.49	VFAINT
3	8608	-	2008-08-05 22:44:39	8.84	351.72303	0.01783	242.49	VFAINT
3	8609	-	2008-08-06 01:19:39	8.84	353.09031	-0.01102	242.49	VFAINT
3	8610	-	2008-08-06 03:54:42	8.84	352.15938	0.30473	242.49	VFAINT
3	8611	-	2008-08-06 06:29:27	8.83	352.01198	0.02339	242.49	VFAINT
3	8612	-	2008-08-06 09:04:08	8.84	351.47375	0.02736	242.49	VFAINT
3	8613	-	2008-08-06 11:38:49	8.84	352.25372	0.06485	242.49	VFAINT
3	8614	-	2008-08-06 14:13:30	8.84	352.80328	0.06085	242.49	VFAINT
3	8615	-	2008-08-06 16:48:28	8.84	351.48138	0.26156	242.49	VFAINT
3	8616	-	2008-08-06 19:23:35	8.83	352.54266	0.05529	242.49	VFAINT

TABLE 2 – continued from previous page

Field	ObsID	Sub-field (UT)	Obs. Start (UT) (ks)	Exp (ks) (deg)	α_{J2000} (deg)	δ_{J2000} (deg)	Roll Angle	Mode
3	8617	-	2008-08-06 21:58:23	8.84	352.42188	0.29140	242.49	VFAINT
4	8619	-	2007-11-28 13:18:37	9.04	36.63964	0.70242	50.76	VFAINT
4	8620	-	2007-11-28 16:09:09	8.66	36.72970	0.48135	50.76	VFAINT
4	8621	-	2007-11-29 01:03:58	9.07	36.88713	0.70250	50.76	VFAINT
4	8622	-	2007-11-29 03:53:59	8.66	37.14407	0.70447	50.76	VFAINT
4	8623	-	2007-11-29 06:32:28	8.66	37.39158	0.70452	50.76	VFAINT
4	8624	-	2007-11-29 09:10:59	8.66	37.63909	0.70268	50.76	VFAINT
4	8625	-	2007-11-29 11:49:28	8.66	37.89038	0.76129	50.76	VFAINT
4	8626	-	2007-12-01 11:55:28	8.86	36.97907	0.48142	50.76	VFAINT
4	8627	-	2007-12-01 14:50:45	8.46	37.22656	0.47393	50.76	VFAINT
4	8628	-	2007-12-01 17:25:55	8.47	37.48350	0.47209	50.76	VFAINT
4	8629	-	2007-12-01 20:01:05	8.47	37.72722	0.47402	50.76	VFAINT
4	8630	-	2007-12-01 22:36:15	8.47	37.88970	0.59744	50.76	VFAINT

NOTES–
[a] XDEEP2 Field number.
[b] *Chandra* observation identification number.
[c] Due to missing gain files within the CALDB, ObsID 6221 is not included in the analyses of Field 1 which are presented here. The exposure time of 6221 is only 4.15 ks, hence, its rejection is relatively insignificant compared to the total exposure time within Field 1 and will have a negligible effect on our conclusions.
[d] Sub-field name for observations in Field 1, adopted from Laird et al. (2009).
[e] Observing date and start time in UT.
[f] Exposure time in kiloseconds after appropriate screening.
[g] Aim point position of observation in degrees in J2000 coordinates.
[h] Spacecraft roll angle in degrees in standard north-east co-ordinate system.
[i] *Chandra* observing mode.

2.2. *Data reduction*

Basic processing was carried out using the *Chandra* X-ray Center (CXC) pipeline software. In addition, further processing of the X-ray data was carried out using the CHAV (v4.3)[10] and CIAO (v4.3) [11] software packages combined with custom IDL scripts. Each ACIS-I observation was analyzed separately. Individual ACIS-I pointings were reduced from the Level-1 event file products of the standard *Chandra* data pipeline. We use the CIAO tool `acis_process_events` to remove the standard pixel randomization, and STATUS=0 was used to remove streak events, bad pixels and cosmic ray afterglow features.

All observations were visually inspected for flaring and periods of high background. The majority of the observations were found to not be significantly contaminated. As also noted in Nandra et al. (2005) and Laird et al. (2009), observation 4365 does exhibit an interval (≈ 25 ks; ~ 30 % of the observation) of elevated background. However, unlike the previous analyses, here we conservatively screen-out this period of high background. Final effective exposures in good-time intervals for each observation were generally found to be > 90 % of the "on-time" (see Table 2).

2.3. *Creation of individual images & exposure maps*

Events files were screened using a standard grade set (GRADE=0,2,3,4,6) to construct images for each individual ObsID. Images were constructed in the Full (FB; 0.5–7 keV), Soft (SB; 0.5–2 keV) and Hard (HB; 2–7 keV) bands at the full ACIS-I spatial resolution, 0.492 arcsec/pixel. Here we limit the photon energy to $E < 7$ keV to allow a more direct comparison to sources detected in the XBootes survey. Given the small effective area of the ACIS-I detector at $E > 7$ keV, relatively few $E > 7$ keV photons are detected, and thus this choice of energy boundary is somewhat arbitrary and will have little effect

[10] CHAV is available at http://hea-www.harvard.edu/~alexey/CHAV/
[11] CIAO is available at http://cxc.harvard.edu/ciao/download/

on our conclusions. The CHAV tool `aspecthist` was used to create aspect histograms in all three bands. These aspect histograms were used to generate exposure maps by convolving them with the standard ACIS-I chip-map (`ccd_id=0,1,2,3`) and reprojecting to the previously created counts images. Reference spectra in monochromatic bands of $E \sim 1.0$, 4.0 and 2.5 keV (i.e., the median energies of the SB, HB and FB, respectively) were used in the creation of the exposure maps.

2.4. *Astrometric calibration & observation merging*

Due to differing observing strategies and the sizes of exposure area overlaps between individual *Chandra* observations within each XDEEP2 field, X-ray observations were combined using separate methods for Field 1 and Fields 2–4. As stated previously, Field 1 contains eight sub-fields (see §2), with marginal overlap (~ 0.01–0.02 deg^2) between one another. Each of these eight sub-fields consists of several (3–28) individual *Chandra* ACIS-I exposures with significant overlap between the observations within a particular designated sub-field. We used the CIAO Perl script, `merge_all` to create contiguous raw X-ray images and exposure maps within each of the eight Field 1 sub-fields. Briefly, this script searches for bright X-ray sources within two events tables which spatially overlap and compares the astrometric co-ordinates of the detected sources. By computing the average offset between the sources within the tables, and guarding against rogue outliers, the events table and associated aspect histograms are reprojected to the world co-ordinate system (WCS) of the first reference observation within the sub-field.

Given the limited area overlap (which occurs only at large off-axis radii) between the eight sub-fields, a resultant merged events table and images from a further use of `merge_all` to combine the sub-fields, is likely to be highly uncertain. However, one of the primary goals for this XDEEP2 X-ray catalog is to compare the X-ray detected sources with the previously astrometrically-calibrated optical DEEP2 catalog presented in Coil et al.
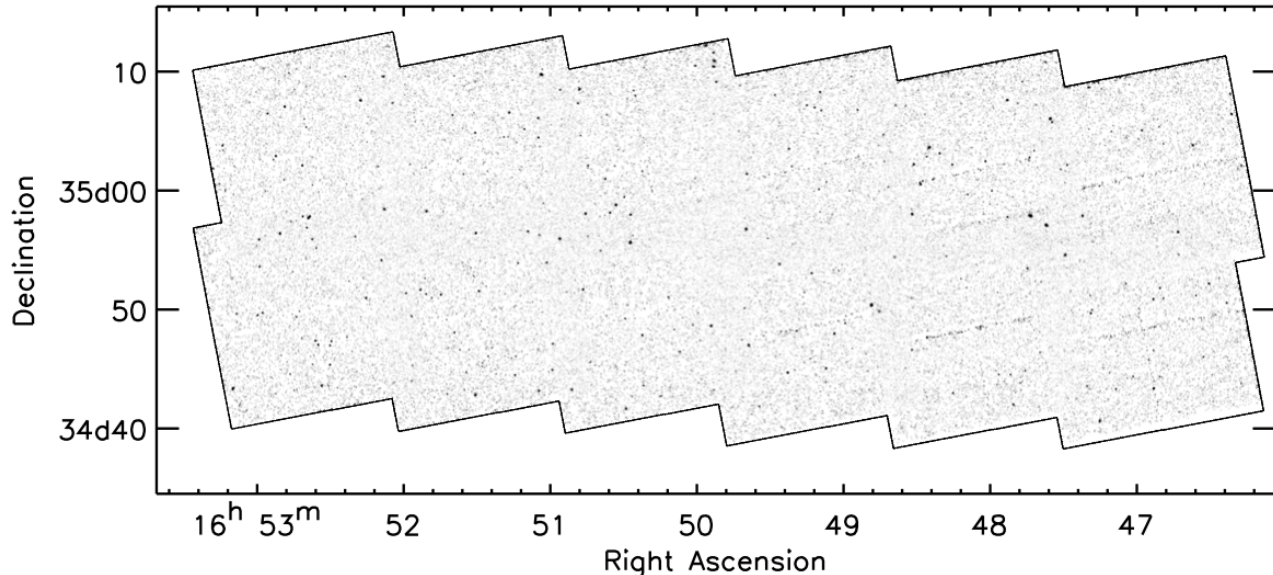
Fig. 2.— Example of a full-band (0.5–7keV) merged raw counts image of an XDEEP2 field. Region shown is Field 2. Individual *Chandra* pointings have been merged using the CIAO tool `merge_all`. The image has been smoothed using a Gaussian kernel for presentation purposes only. Many sources are clearly evident throughout the image. Due to the presentation smoothing process, edge-effects (correlated streaks) can be seen along the positions of the chip gaps.
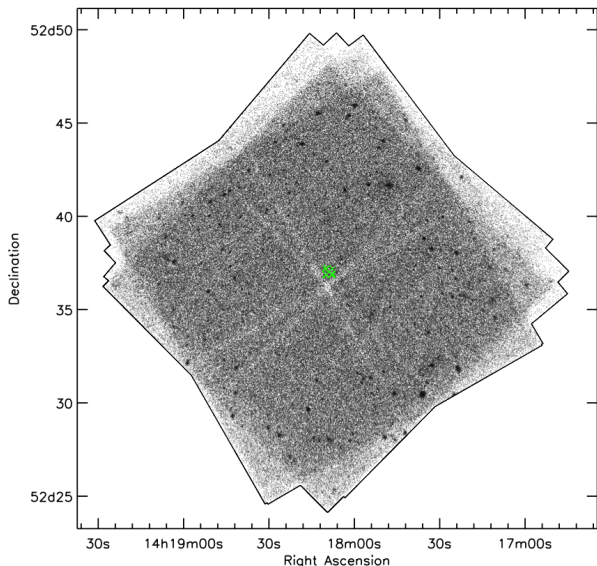

Fig. 3.— Merged source count image of the sub-field AEGIS-3 located in Field 1. Aim points of the individual *Chandra* ObsIDs within the sub-field are shown with green crosses matched to the roll angle of the space craft. The angular separation of the aim-points is sufficiently small (~ 5 arc-seconds) that they allow for combining of the individual ObsIDs into stacked images.

(2004). Hence, we may consider the WCS astrometry of the DEEP2 optical catalog to be an absolute reference frame. Thus, here we use the DEEP2 optical source positions to correct the X-ray sub-fields for any systematic offsets that may be present in the combined X-ray data. Following Brand et al. (2006), we use a counterpart-matching algorithm (described in detail in § 5 of this manuscript) to match X-ray sources detected within 3 arc-minutes of the nominal observation aim-point to op-

tical counterparts. We calculated the median offset between the X-ray and optical positions for the respective sources to identify any necessary translation for the X-ray sub-fields. We present these offsets and their associated rms uncertainties in Figure 1. Typically, ~ 20–30 X-ray–optical sources were used to determine the necessary translations; the offsets were generally found to be < 0.25 arc-seconds (i.e., $\sim 50\%$ of the ACIS-I pixel scale). While rotations were also allowed in the calculation of the relative astrometries, the magnitude of the angular rotation was always found to be negligible ($\ll 1$ degree) and consistent with no rotation. Hence, we did not include angular rotations and used only linear transformations for the final corrections of the X-ray WCS to that of DEEP2. The required positional offsets for the merged X-ray images were applied using the CIAO tool `wcsupdate`. The CIAO tool `reproject_aspect` was used to reproject the events table and aspect solution files.

In Fields 2–4, the relatively shallow 9–10 ks X-ray observations include little or no overlap area between exposures. As such, and similar to the merged sub-fields in Field 1, `merge_all` cannot be used to accurately co-align the relative astrometries within the individual X-ray observations in these three fields. Hence, again we consider the WCS reference frame of the optical DEEP2 catalog to be absolute, and use the optical sources to align individual X-ray observations following the same methodology described above. Given the far shallower depth of the X-ray observations in Fields 2–4, we include all X-ray sources with optical counterparts to a distance of < 5 arc-minutes from the aim-point. This larger off-axis distance encompasses sufficient X-ray–optical source numbers (5–20 per observation) to accurately constrain any required systematic astrometric correction. Four of the *Chandra* ObsIDs (8637; 8614; 8604; 8628) included five or fewer X-ray–optical sources, and hence we consider any astrometric corrections for these four observations
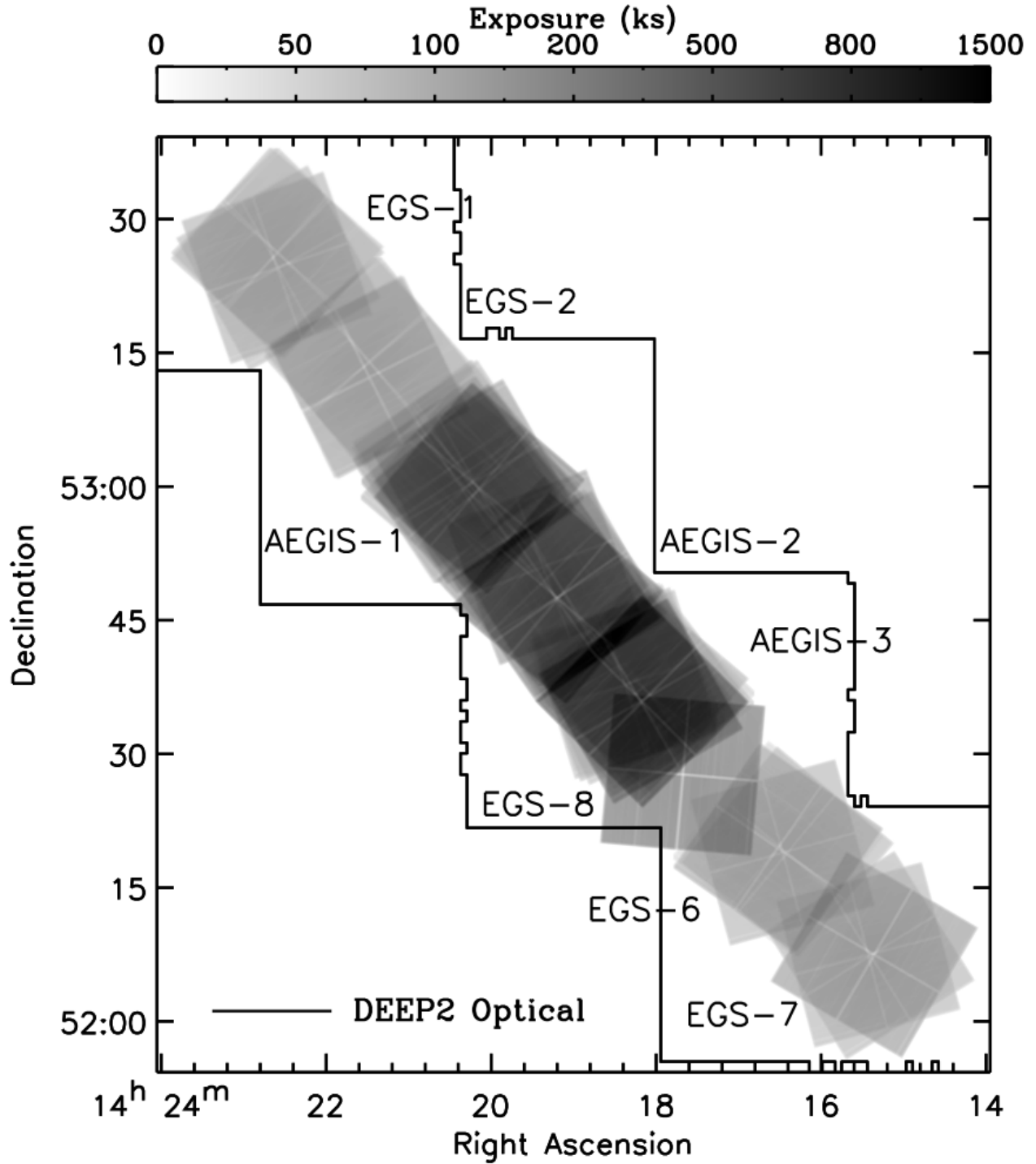
FIG. 4.— Merged full-band (0.5-7 keV) *Chandra* ACIS-I exposure map for XDEEP2 Field 1. Reference spectra in monochromatic bands of $E \sim 1.0$, 4.0 and 2.5 keV and a spectral slope of $\Gamma = 1.7$ were assumed in the creation of the exposure maps from the aspect histograms. The effective exposure (and hence sensitivity depth; see §4.1) across Field 1 is non-uniform and varies dramatically from ≈ 20 ks–1.1 Ms due to the large number of overlapping observations. Overlaid is the nominal survey area covered by the DEEP2 Galaxy Redshift Survey optical observations (solid black line).
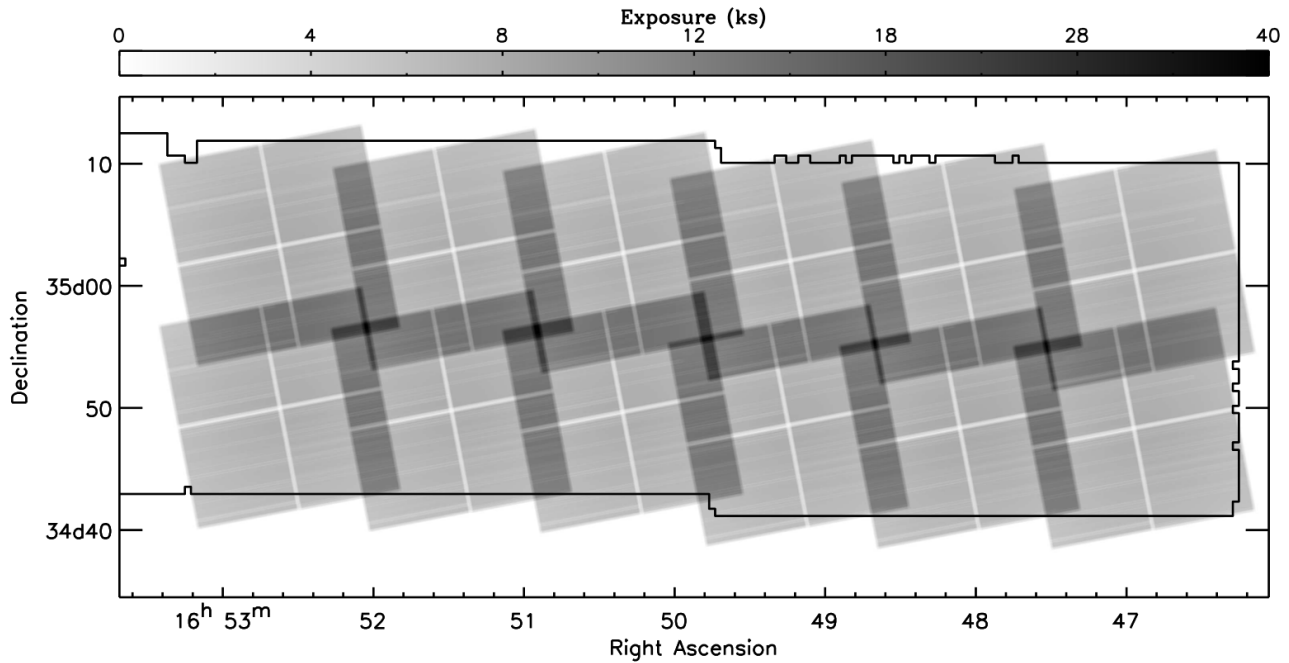
FIG. 5.— Same as Fig. 4, except field shown is XDEEP2 Field 2
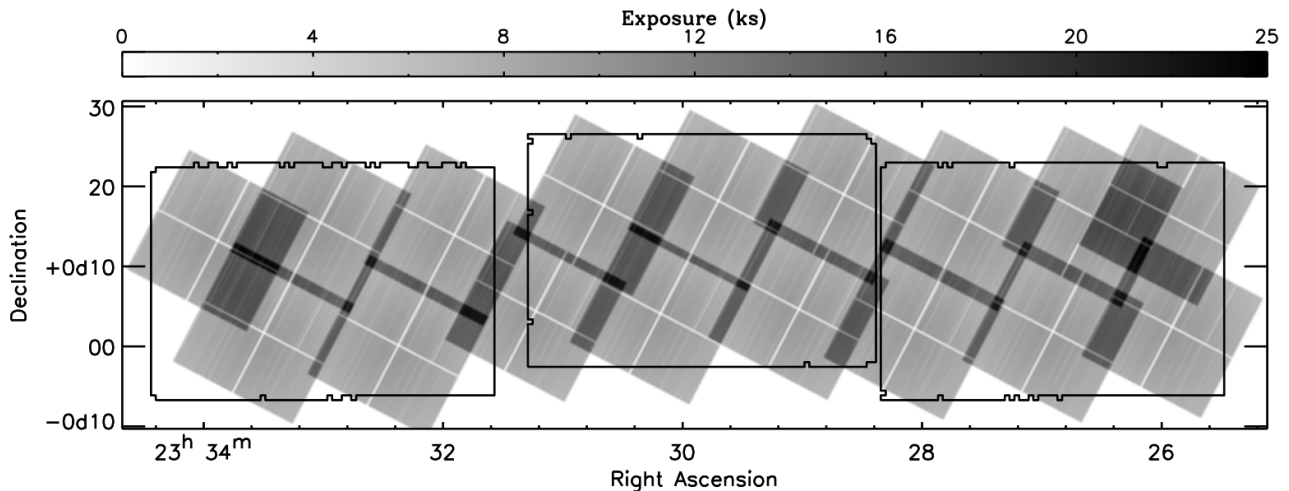
FIG. 6.— Same as Fig. 4, except field shown is XDEEP2 Field 3

to be sufficiently uncertain that we subsequently include all detected X-ray sources (at all off-axis distances within the observation) to further constrain any median offset. The calculated median offsets and associated uncertainties are also included in Figure 1. Clearly, using our adopted methodology, we do not account for any possible field-to-field (or intra-field) variations in the astrometric accuracy of the optical DEEP2 catalog. However, given the low number of X-ray sources within individual *Chandra* observations, further investigation and/or necessary correction to the DEEP2 catalog are beyond the scope of this study. Overall, the required astrometric corrections (average correction of 0.24") for the whole of XDEEP2 are consistent, if not slightly lower, than those found in previous wide-field X-ray surveys (e.g., XBootes: 0.41";

Brand et al. 2006) and can be considered sufficiently precise for our purposes.

2.5. *Merged XDEEP2 field maps*

In Figures 2 and 3, we show examples of the merged full-band (0.5–7 keV) counts images and in Figures 4–7, we present the merged full-band exposure maps for the four survey fields. As shown in Figure 8a, the effective exposure (and hence sensitivity depth; see § 4.1) across Field 1 is non-uniform and varies dramatically from ≈20 ks–1.1 Ms. The effective exposure in Field 1 is dependent on the number of repeat exposures, the large number of overlapping regions and the varying spacecraft roll-angles between separate pointings. We show that at the 80th percentile, the effective exposure in
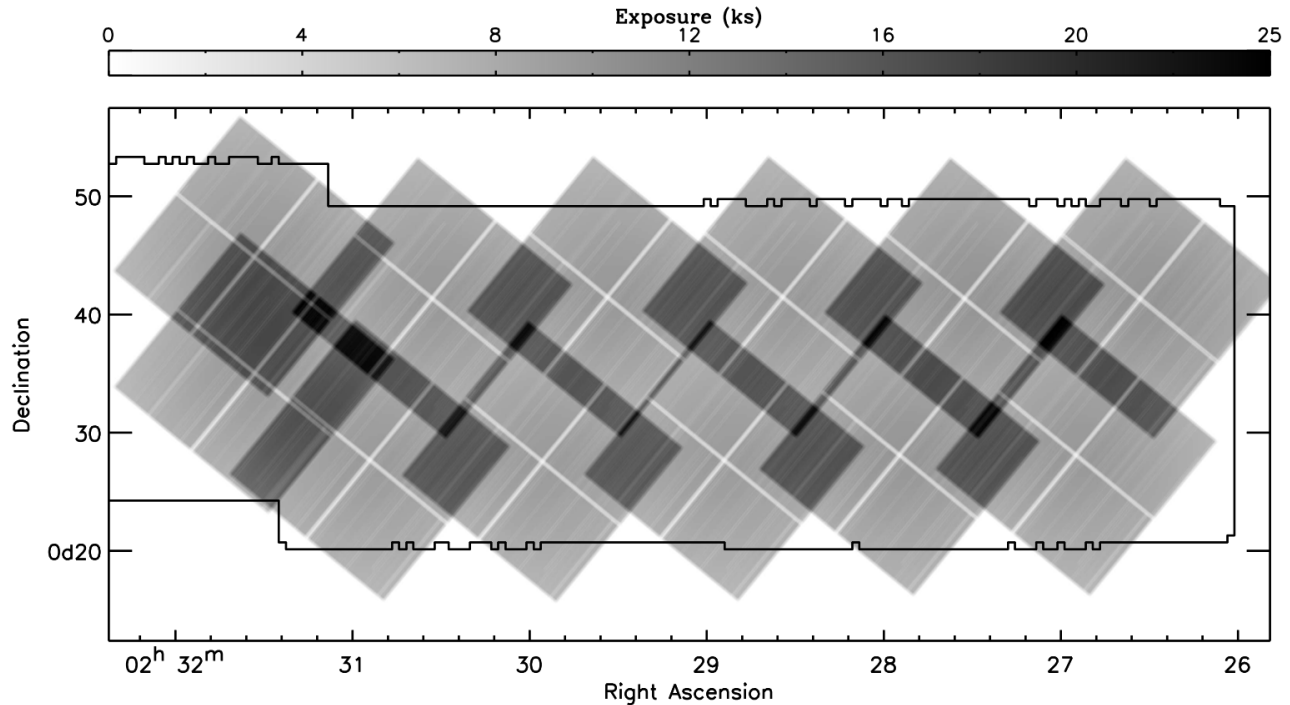
FIG. 7.— Same as Fig. 4, except field shown is XDEEP2 Field 4

Field 1 is ≈140 ks. By contrast, the effective exposures in Fields 2, 3 and 4 are relatively uniform (~ 9 ks at 80%) with constant spacecraft roll angle and only small overlap regions between the individual ACIS-I pointings ($< 20\%$). In Figure 8b, we also show the effective exposure time across the combined XDEEP2 area and compare this to the *Chandra*-COSMOS (Elvis et al. 2009) and Extended-*Chandra* Deep Field South fields (Lehmer et al. 2005). It is clear that XDEEP2 complements these previous surveys: the survey depth of XDEEP2 extends well beyond ~ 200 ks (the limiting effective exposure of the E-CDF-S) to > 600 ks at similar survey area ($A \sim 0.2$ deg^2); and XDEEP2 covers a survey area which is a factor ≈ 4 greater than that of *Chandra*-COSMOS.

The raw merged count images for each of the four XDEEP2 fields were adaptively smoothed using custom IDL software based on the kernel-smoothing program, ASMOOTH (Ebeling et al. 2006). Given the wide range in exposure times across Field 1, we include a weighting algorithm based on the average number of counts within binned background images (see §4.1) to account for changes in background count rate in overlapping regions. This background-weight is applied to the calculation of the smoothing radii within our custom version of ASMOOTH. The smoothing scales, which are calculated from analysis of the merged counts images, are then applied directly to the respective exposure maps. We use these to create false-color exposure-corrected smoothed images in each field (see Figure 9).

3. POINT SOURCE DETECTION & SPURIOUS SOURCES

In this section we outline the methods used to detect point-like sources throughout the XDEEP2 fields. Following earlier analogous methods for numerous wide-field and deep X-ray surveys, we used wavelet decomposition software to detect sources across XDEEP2. Indeed, previous analyses of Field 1 have used the CIAO tool wavdetect to detect X-ray source candidates. Here, we chose to use wvdecomp which is publicly available in the ZHTOOLS package (see Vikhlinin et al. 1998). In §4.2 we perform a comparison of the X-ray sources detected in Laird et al. (2009) which used wavdetect and additional signal-to-noise criteria to the sources detected in this work using wvdecomp. Briefly, we find little or no difference between the number of sources detected in either analyses. We find that $\sim 96\%$ of the unique X-ray sources found in the previous AEGIS-X catalog are included in our new catalog (presented here) which now includes the more recent longer exposure ACIS-I observations. We find that the majority of the sources which are not included in our new catalog are relatively low significance with few counts (< 10) and, in general, are detected in only one energy-band in the Laird et al. catalog. Sources similar to these were conservatively removed as possibly spurious detections in our new catalog based on our extensive MARX simulations (see §3.4).

3.1. *Point source detection in individual Chandra ObsIDs*

Point sources were detected in the individual (non-merged) counts images for the SB, HB and FB energy ranges. We used a point source detection threshold in wvdecomp of 4.5σ (equivalent to a probability threshold of 1×10^{-6}). Point sources were detected over wavelet scales of $\{1, \sqrt{2}, 2, 4\} \times 0.492''$. After detection of a source candidate, the event data at the approximate wavelet position was iterated up to five times to accurately determine the final events centroid, and hence, source position. In Figure 10, we present the offset dis-
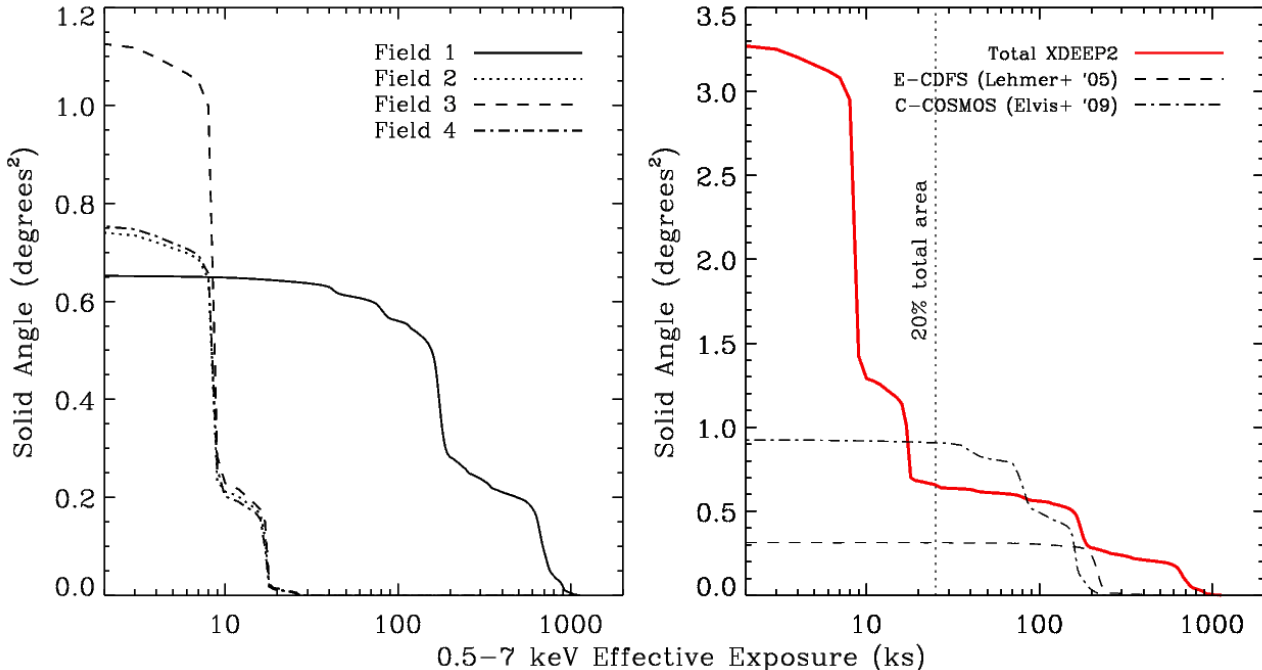
Fig. 8.— **a (left):** Cumulative survey solid angle (in degrees) as a function of effective exposure in the full-band (0.5–7keV) for the four separate XDEEP2 fields. **b (right):** Total effective exposure across the combined XDEEP2 survey compared to the E-CDFS (Lehmer et al. 2005) and C-COSMOS (Elvis et al. 2009) survey fields. Minimum effective exposure for 20% of the total XDEEP2 area is highlighted with a dotted line.

tances between the wavelet and event centroid positions. We find that $> 90\%$ of the X-ray sources have offset distances $\lesssim 0.3$" from the wavelet position. Indeed, the vast majority of the sources are consistent with zero offset. Furthermore, we find that the median offset distance between the wavelet and centroid positions are mildly correlated with the on-chip distance of the source from the observation aim-point. Those sources at $d_{OAX} < 5$' have Δ(wavelet $-$ centroid) ~ 0.2", while those sources closer to the edge of the FOV, at $d_{OAX} \gtrsim 10$', have Δ(wavelet $-$ centroid) ~ 0.65". These increased offsets at large off-axis distances were most likely due to asymmetries in the ACIS PSF shape.

Source lists, generated from the separate energy bands in the individual observations, were cross-correlated based on their source positions. Two-dimensional Gaussian profiles were used to represent the sources detected in the separate energy bands with full-width half maxima (FWHM) determined by the physical size of the 90% encompassed energy fraction (EEF) within the *Chandra* energy-band images with the assumption of a spherically symmetric model for the ACIS-I PSF. The centers of the Gaussian profiles were allowed to shift within the 1σ centroid error (see §3.3) of the source positions to maximise the statistical likelihood of a source match. A unique source was determined to exist when the summed 2-D Gaussian profile was well-fit at the 90% confidence level by a single (approximately symmetrical) 2-D Gaussian profile with FWHM $< 90\%$ EEF.[12] This methodology has the advantage that the 'matching-radius' naturally becomes a function of both the off-axis position and the energy-band of the source detection. Hence, it incorpo-

rates the size increase and rotation of the ACIS-I PSF radius which, while assumed to be symmetrical about the aim-point, still increases significantly for large off-axis distances and simultaneously changes as a function of both azimuthal angle and effective energy.

3.2. *Sources in overlapping observations in Field 1*

As stated previously, sources were detected in each of the individual ObsIDs. In Fields 2,3 and 4 there are small regions of significant exposure (> 10 ks), where individual observations overlap. However, given the large systematic uncertainties brought about by significant differences in *Chandra* PSF radii, we did not attempt to combine these observations to search for faint sources, which would be detected in the merged deeper exposure regions. Instead, where duplicate sources in these overlap regions appear (see previous section), the source which is radially closest to the aim point in a particular *Chandra* observation (i.e., the source which has the smallest point spread function), is included as a unique source in the final catalog. By contrast, given the large overlap between the *Chandra* observations in the sub-fields of Field 1, it is highly likely that the same physical X-ray source is detected in multiple individual exposures and that many fainter sources would be detected in merged X-ray images. Hence, we have created merged events files of the sub-field regions, which were defined in Laird et al. (2009) (see Table 1 of Laird et al. 2009 and Table 2 and Figure 3 in this work).[13]

When combined, the Field 1 'EGS' sub-fields show a significant increase in the overall exposure and depth. Each of the observations in these sub-fields have varying

---

[12] We use the IDL routine `mpfit2dpeak`, available in the Markwardt software package, to fit the 2-D Gaussian profiles.

[13] We note that the analyses presented here now include the new 600ks observations in the sub-fields EGS-3, EGS-4 and EGS-5.
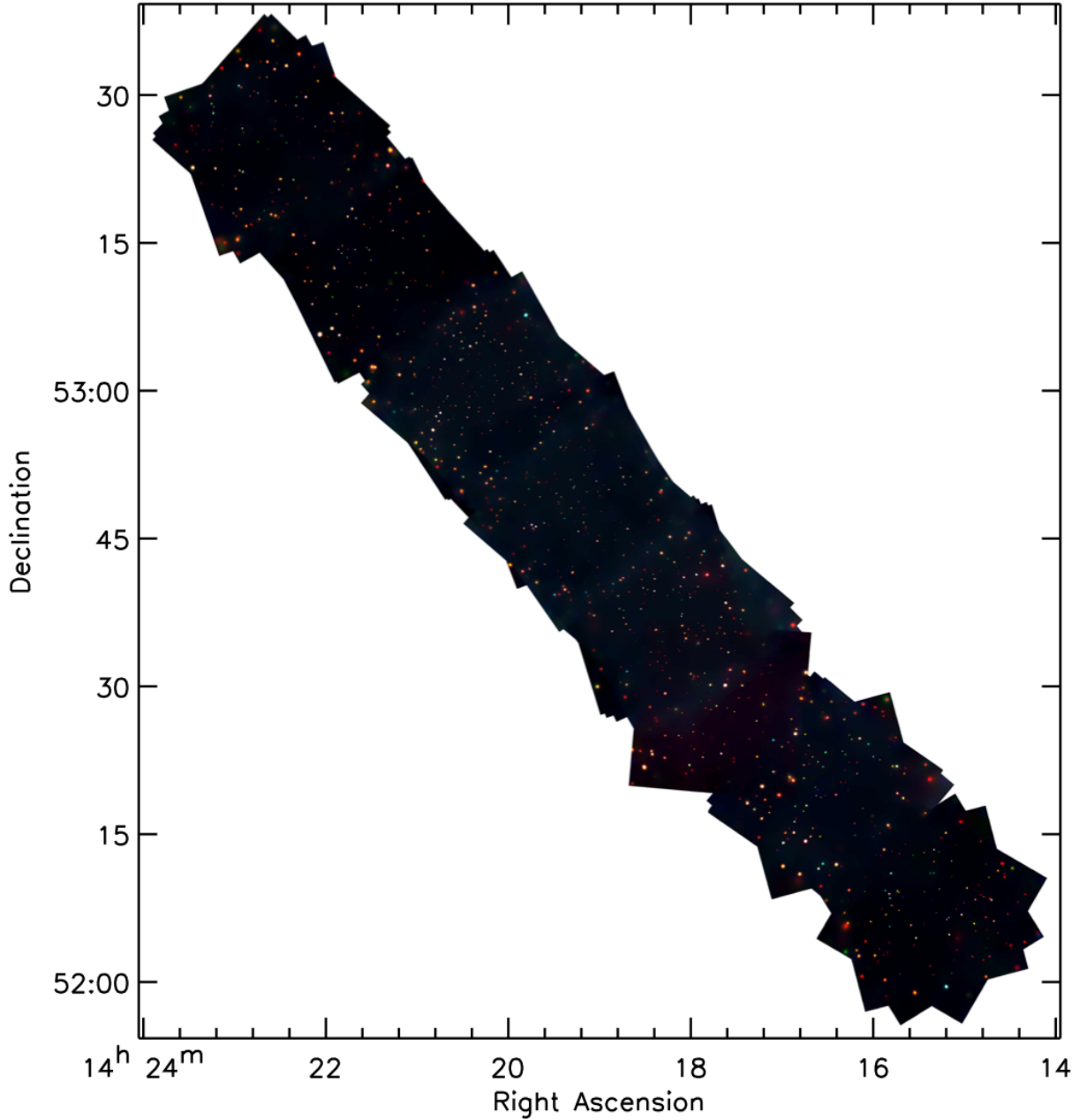
FIG. 9.— *Chandra* false color image of XDEEP2 Field 1. The image is a merged composite of the exposure corrected 0.5–2 (red), 2–4 (green) and 4–7 keV (blue) images within Field 1. The color-band images have been adaptively smoothed with varying smoothing scales determined from the average background counts in the stacked images.

space-craft roll angles. However, as shown in Table 2, the pointing co-ordinates are similar ($\lesssim 5$ arc-seconds; see also Figure 3). As such, these stacked sub-fields do not suffer from significant sensitivity degradation due to large changes in the *Chandra* point spread function (i.e., the observational setup was similar to that of the CDF-N and CDF-S; e.g., Alexander et al. 2003a; Xue et al. 2011). We used wavelet decomposition to search for additional faint sources in these *merged* (stacked) sub-field images which would otherwise not be detected in the individual observations. Candidate source lists for Field 1, which were compiled from each of the individual ObsIDs and those lists derived from the merged sub-field images were compared using the same unique-source detection

method outlined in the previous section. The final unique source position and associated centroid errors were determined by averaging and combining in quadrature the previously calculated positions and uncertainties in the individual and merged X-ray observations.

3.3. *Source extraction*

Once the unique source locations were determined across each of the XDEEP2 fields, we counted the number of events ($C_{50,\mathrm{SB/HB/FB}}$, $C_{90,SB/HB/FB}$) within the 50% (R_{50}) and 90% (R_{90}) encircled energy fraction regions of the merged sub-field images (Field 1) and the individual ACIS-I observations (Fields 2–4) for each of the soft, hard and full bands. Within the sub-fields of
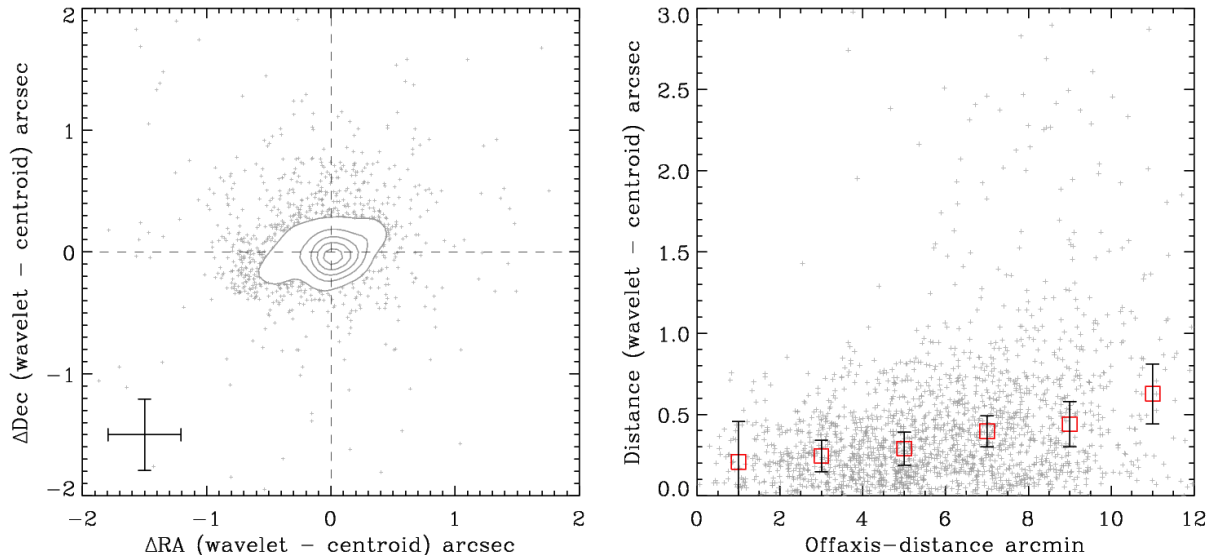
FIG. 10.— **a, left:** Positional offsets between the wavelet-centers produced from `wvdecomp` and the events centroids. Contours encompass 50, 65, 80, 90 and 95% of XDEEP2 sources. We find a small systematic offset of < 0.1" between the median source positions produced from the events centroid and wavelet center methods. Median 90% uncertainties of ±0.3" were derived following Murray et al. (2005), see §3.3. **b, right:** Angular separation (wavelet – centroid) as a function of off-axis distance for XDEEP2. Median offset distances and the associated median RMS scatter are given in bins of 2' (open squares).

Field 1, the radii for circular extraction regions were calculated from the off-axis radial distances in PSF simulations. We used the MARX simulator to model a point-source, within a specific energy-band, at varying roll angles and off-axis distances from an observation aim-point. The modeled energy-band images were combined using the method outlined in §2.4, and the spatial extent of the merged point-source was measured using a circular aperture to determine accurate extraction radii for the candidate sources identified in the Field 1 sub-fields.

We calculated average effective exposures for each candidate source in the R_{50} and R_{90} extraction regions. Background counts were determined for each source by extracting photon counts in annuli at inner and outer radii $\{1.1, 2.5\} \times R_{90}$, respectively, in background images (see §4.1). Background counts were scaled by the ratio of the areas of the EEF extraction region and the background extraction region. Scaled background counts were subtracted from the respective C_{50} and C_{90} to give final net source counts ($C_{50,\mathrm{net}}$; $C_{90,\mathrm{net}}$, respectively). The 50% and 90% encircled energy fraction regions were chosen to match those used in the XBootes survey (Murray et al. 2005; Kenter et al. 2006; Brand et al. 2006) allowing direct comparisons to be made between the catalogs in future publications.

For a source detected in a particular energy band image, we computed the total number of source counts in the other energy band images using the analyses described above. We converted the net count rates in each band (SB; HB; FB) to total fluxes (F_{SB}; F_{HB}; F_{FB}, respectively). To build a homogeneous X-ray catalog, we assumed a single simple absorbed power-law spectrum with $\Gamma = 1.7$ (i.e., the typical intrinsic slope of an AGN) for all sources and $N_{\mathrm{H}} = \{1.24, 1.75, 3.99, 2.89\} \times 10^{20} \, \mathrm{cm}^{-2}$ for those sources in Fields 1, 2, 3 and 4, respectively. Here, we use PIMMS to calculate the count-rate–flux conversion factors assuming the simulated ARFs from AO9 of the *Chandra* program. The use of the AO9 ARFs compared to AO6 results in a $\sim 4\%$ decrease in the calculated 0.5–7 keV flux. Total galactic HI column densities were determined using Stark et al. (1992). Uncertainties on the counts and fluxes were calculated using the formalism of Gehrels (1986).

Following Murray et al. (2005), we estimated the 90% uncertainty on the source locations as $X_{\mathrm{err}} = R_{50}/(C_{50}^{1/2} - 1)$. For those sources with $C_{50} \leq 5$ counts, we set a minimum centroid error of 0.8 arc-seconds (i.e., the 99% positional accuracy on the ACIS-I detector[14]), which takes into account the systematic uncertainties associated with the space-craft and detector astrometry. Random uncertainties also become negligible for sources with large numbers of counts.

3.4. *Spurious sources*

Given the widely varying exposure times, and hence varying background levels of individual observations within XDEEP2, it is important to apply further restrictions to the detected-source lists based on the number of counts for a given source. For those observations with large exposure times, the number of spurious sources with seemingly low numbers of counts increases (see Figure 11a). To limit the number of spurious sources within our final catalog, we applied a minimum photon count threshold of $n_{\mathrm{counts}} > n_{\mathrm{cut}}$, where n_{cut} was determined through simulations of sourceless background ACIS-I images. We used the MARX software package to simulate 100,000 *Chandra* ACIS-I images of the unresolved Cosmic X-ray background (XRB), including instrumental effects for exposure times of 3, 6, 9, 12, 15, 20, 30, 50, 75 and 100ks. To approximate the expected emission from the unresolved CXB, we employed a simple absorbed power-law spectrum with $\Gamma = 1.4$ (e.g., Hickox & Markevitch 2006) and $f_X \sim 8.189 \times 10^{-13} \, \mathrm{erg \, s}^{-1}$ in
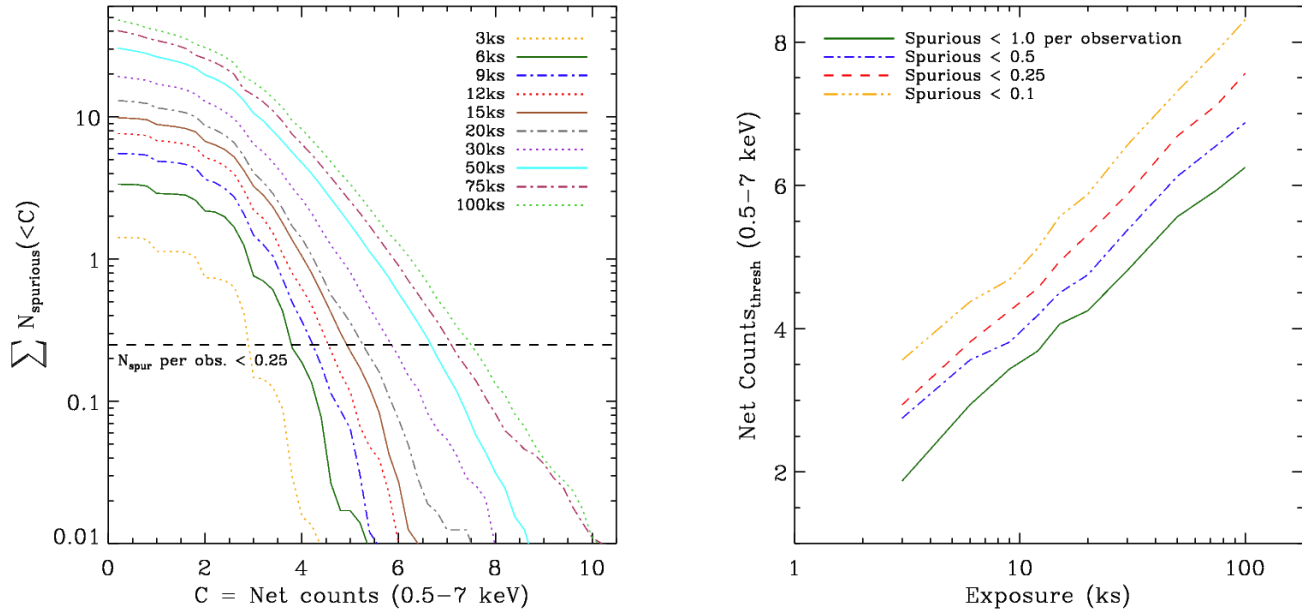
---

[14] see http://cxc.harvard.edu/cal/ASPECT/celmon/

FIG. 11.— (a; left) Average total number of spurious sources (N) detected in MARX simulated background images as a function of net photon counts in the full-band (C) measured in the spurious source. (b; right) Required net count threshold to ensure the average total number of spurious sources (derived from Monte-Carlo simulations) are < 0.1; 0.25; 0.5; 1.0 (dot-dot-dash line; dash line; dot-dash line; solid line, respectively) in a *Chandra* ACIS-I observation plotted as a function of exposure time in kiloseconds.
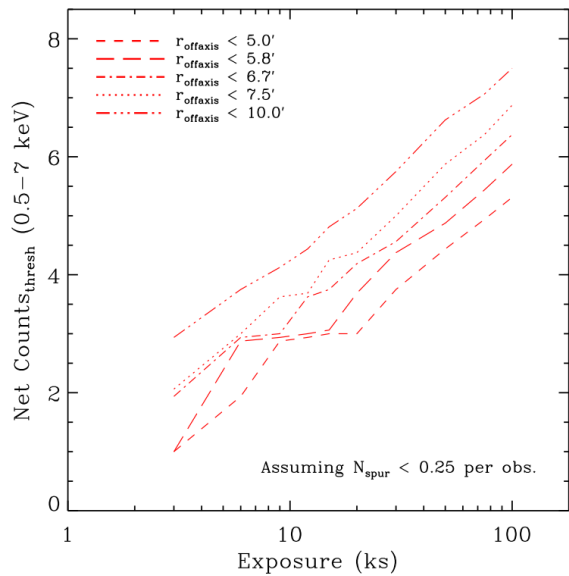

FIG. 12.— Source count threshold cut in the 0.5–7 keV band as a function of exposure time in MARX simulated *Chandra* ACIS-I imaging. For a fixed total number of spurious sources of $N < 0.25$ within simulated observations, we show the dependence of the threshold cut on the off-axis position of the detected spurious sources.

the 0.5–7 keV band; i.e., the XRB surface brightness measured in the ROSAT all-sky survey in a blank-sky region of XDEEP2 Field 1, which was then scaled to the projected area of ACIS-I. We note that this simplification assumes the CXB emission is homogeneous across an ACIS-I observation. We searched each of the simulated XRB ACIS-I images for spurious sources using the same wavelet detection thresholds defined above (see Figure 11a). To build source lists which were both relatively complete while limiting the number of spurious sources,

we cut the source-lists where the expected total number of spurious sources Σn for a given exposure i was $\langle \Sigma n_i \rangle < 0.25$ (see Figure 11b). By adopting a threshold of $\langle \Sigma n_i \rangle < 0.25$, we expect a spurious source detection rate of $< 1\%$ in the final catalog.

As we show in Figure 12, we find that the spurious net count threshold is both a function of exposure time $(t_{\rm exp})$ and off-axis position $(x_{\rm OAX[']})$ of the source within an ACIS-I observation. This count threshold can be approximated by the empirical formula,

$$n_{thresh} = -\frac{5}{3} + \frac{3}{10}x_{\rm OAX} + \frac{ln[60x_{\rm OAX} - 30]}{2}\log t_{exp} \quad (1)$$

and we use this to derive n_{thresh} for a given fixed off-axis position and exposure. To verify that this parametrization of the count threshold can be extrapolated to larger exposure times (i.e., for the merged AEGIS-1, 2 and 3 sub-fields in XDEEP2 Field 1), we simulated 100 1 Ms ACIS-I exposures using MARX. On average, we detected < 1 spurious source in each 1 Ms simulation by using $n_{thresh} > 20.3$. Hence, within the Poisson error, we detected the same number of spurious sources expected when extrapolating the above equation to $t_{exp} = 1$ Ms. By conservatively adopting a threshold of $\langle \Sigma n_i \rangle < 0.25$ across the 126 XDEEP2 pointings we expect $\lesssim 30$ spurious sources in the final XDEEP2 catalog.

4. THE XDEEP2 CATALOG

The XDEEP2 point source catalog contains 2976 unique sources, with 1720, 342, 528 and 386 sources in Fields 1, 2, 3 and 4, respectively. For the purposes of our point source catalog, we do not discuss those sources which are extended (e.g., the galaxy clusters) as these will be the subject of a future publication. In Table 5 we show a short extract from the main source table, which is available electronically. In Figure 13, we show the distribution of source counts across the four XDEEP2 counts
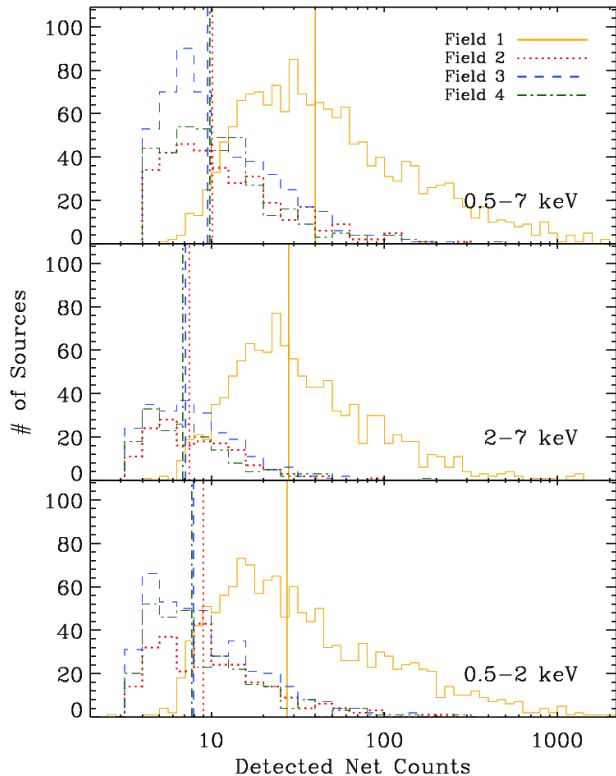
FIG. 13.— Distribution of X-ray counts for sources detected in each of the four XDEEP2 fields in the full-band (0.5–7keV; top panel), hard-band (2–7keV; middle panel), and soft-band (0.5–2keV; bottom panel). Median source counts for each energy band in the associated field are shown with vertical lines.

TABLE 3
SOURCES DETECTED IN SEPARATE ENERGY BANDS

Detection band [a] (keV)	#	Non-detection band [b]		
		Full	Soft	Hard
Full	2849	-	661	1196
Soft	2301	111	-	1006
Hard	1663	12	372	-

NOTES–
[a] Energy band which a source has been detected in
[b] Number of sources where there is a non-detection in a particular energy-band when it has been detected in a different band.

in the soft, hard and full bands. It is clear that both the wide-spatial area of XDEEP2 combined with the smaller regions of sensitive long-exposures, are extremely complementary to one another. A significant cut-off is observed for sources with $C_{90,\mathrm{SB}} \lesssim 9$ in Field 1 since relatively few sources (~ 100) are detected with 5–10 counts within R_{90} due to the long integrated exposures, even in the soft-band. However, many more sources, down to $C_{90,\mathrm{FB}} \sim 5$ are detected when the other three XDEEP2 fields are included. Hence, within the point source catalog we detect sources down to ~ 4 net counts in the SB, with a completeness to 20 net counts in the HB and 15 counts in the FB. Furthermore, we detect 70 rare bright sources with $C_{90,\mathrm{FB}} > 500$, which is due to the advantage of the wide-area across the XDEEP2 survey.

In Table 3 we show the breakdown of the numbers of sources detected and formally undetected in individual energy bands within the main XDEEP2 source catalog. Those X-ray sources which are not formally detected in a particular energy band are denoted by "-1" in the relevant net count and flux error columns of Table 5 (e.g., NET COUNTS ERROR SB/HB/FB and FLUX ERROR SB/HB/FB). For these 'non-detections', we use the formalism of Gehrels (1986) to derive 3σ upper-limits from the number of counts observed in the background images (see § 4.1) within the source region. There upper-limits are given in the appropriate NET COUNT and FLUX energy-band columns.

4.1. Background & sensitivity analysis

As is clearly evident from the merged exposure maps, many of the XDEEP2 ObsIDs spatially overlap with one another; however, a subset of these observations, specifically in Field 1, were performed up to seven years apart. Hence, care was taken to analyze changes between the overlapping images as a result of the physical changes in the detector and varying background levels. Background images were constructed separately for each ObsID in the SB, HB and FB energies. Source counts for candidates which were identified as being significant in a particular energy-band using wvdecomp were masked. Background annuli, with inner radii $1.1 \times R_{90}$ and outer radii $5 \times R_{90}$ centered at the source position, were used to calculate the mean local background surrounding the candidate source. The masked source region was re-populated with Poisson noise with a mean distribution equal to that of the local background. The same procedure was additionally used to create background maps of the merged sub-fields in Field 1. While this procedure will remove the count contributions from all point-sources, it will not remove extended emission from sources such as clusters (e.g., Bauer et al. 2002). Hence, the background count levels derived from this method are somewhat conservative, as they will be slightly over-estimated.

The mean background counts, their associated standard deviation and total number of background counts for each field (and sub-field) are shown in Table 4. As expected, the average background counts are a factor of ≈ 15–50 greater in Field 1 than those in Fields 2–4, owing to the much longer exposure times in Field 1. We find that the average backgrounds appear to be relatively stable across the deep sub-fields AEGIS-1 and AEGIS-2, with a slightly higher ($\approx 15\%$) average background count in AEGIS-3. However, we note that the observations in AEGIS-3 occurred 6–12 months after those observations in AEGIS-1 and AEGIS-2. The background levels in XDEEP2 Fields 2, 3 and 4 are almost identical for each of the three energy-bands.

For the purposes of comparing the X-ray point sources detected within each of the XDEEP2 fields, as well as comparing with previous X-ray surveys, it is important to understand the flux sensitivity limitations of a particular X-ray field. The faintest sources detected in the XDEEP2 fields have $f_{\mathrm{X,SB}} \sim 3.1 \times 10^{-17} \, \mathrm{erg \, cm^{-2} \, s^{-1}}$ and $f_{\mathrm{X,HB}} \sim 1.2 \times 10^{-16} \, \mathrm{erg \, cm^{-2} \, s^{-1}}$. While these fluxes are good indicators of the ultimate sensitivity of the survey, sources similar to these may only be detected in stacked images close to the center of several ObsID aim-points where exposure levels are sufficiently high (~ 800 ks) and the combined PSF is relatively small. Hence, given an observing strategy with varying levels of

TABLE 4
BACKGROUND ANALYSIS OF XDEEP2 FIELDS

Field #[a]	Sub-field[b]	Energy band[c]	Mean background [d] (counts pixel^{-1})	Background σ [e] (counts pixel^{-1})	Total Background [f] (10^4 counts)
1	AEGIS 1	Full	0.0841	0.2898	52.5
1	AEGIS 1	Soft	0.0242	0.1539	15.1
1	AEGIS 1	Hard	0.0599	0.2425	37.4
1	AEGIS 2	Full	0.0842	0.2900	51.6
1	AEGIS 2	Soft	0.0236	0.1524	14.5
1	AEGIS 2	Hard	0.0605	0.2448	37.1
1	AEGIS 3	Full	0.0991	0.3033	61.3
1	AEGIS 3	Soft	0.0284	0.1609	17.6
1	AEGIS 3	Hard	0.0706	0.2548	43.7
1	EGS 1	Full	0.0243	0.1438	13.1
1	EGS 1	Soft	0.0070	0.0773	3.8
1	EGS 1	Hard	0.0165	0.1186	8.9
1	EGS 2	Full	0.0235	0.1419	12.0
1	EGS 2	Soft	0.0068	0.0765	3.5
1	EGS 2	Hard	0.0159	0.1167	8.1
1	EGS 6	Full	0.0271	0.1531	14.8
1	EGS 6	Soft	0.0077	0.0815	4.2
1	EGS 6	Hard	0.0184	0.1257	10.0
1	EGS 7	Full	0.0241	0.1429	13.3
1	EGS 7	Soft	0.0070	0.0769	3.9
1	EGS 7	Hard	0.0163	0.1176	9.0
1	EGS 8	Full	0.0332	0.1684	14.7
1	EGS 8	Soft	0.0111	0.0980	4.9
1	EGS 8	Hard	0.0202	0.1310	8.9
2	-	Full	0.0018	0.0428	11.1
2	-	Soft	0.0005	0.0231	3.2
2	-	Hard	0.0013	0.0361	7.9
3	-	Full	0.0018	0.0432	7.4
3	-	Soft	0.0005	0.0234	2.1
3	-	Hard	0.0013	0.0363	5.2
4	-	Full	0.0018	0.0431	7.6
4	-	Soft	0.0005	0.0231	2.2
4	-	Hard	0.0013	0.0364	5.4

NOTES–
[a]XDEEP2 field number
[b]XDEEP2 sub-field name
[c]X-ray energy band of background image: Full 0.5–7keV; Soft 0.5–2keV; Hard 2–7keV
[d]Mean number of background counts per pixel within the non-zero exposure area of the merged images.
[e]Standard deviation of the background counts within the merged images.
[f]Total number of background counts within the merged images.

exposure across the fields, X-ray sources at these low flux levels cannot be uniformly detected across the whole of each field. To quantify the expected number of sources as a function of survey area, we have constructed flux sensitivity maps for each merged field in the 0.5–2 keV, 2–7 keV and 0.5–7 keV bands.

Maps of the *Chandra* point spread functions for an enclosed energy fraction of 90% were simulated at $E \sim 1.0$, 4.0 and 2.5 keV (mean SB, HB and FB energies, respectively) for each ObsID using the CIAO tool `mkpsfmap`. These maps were then merged for all overlapping fields to calculate the mean R_{90} in each image pixel for a merged counts image in the soft, hard and full-bands. We used the formalism of Lehmer et al. (2005) and employed a Poisson model to calculate the average number of counts (N) required to detect a source in a given image pixel for the background counts (b) enclosed within the mean R_{90} calculated in the merged PSF model,

$$\log(N) = \alpha + \beta\log b + \gamma(\log b)^2 + \delta(\log b)^3 \qquad (2)$$

where $\alpha = 0.967$, $\beta = 0.414$, $\gamma = 0.0822$ and $\delta = 0.0051$ (Lehmer et al. 2005). Using equation 2 we convolve the merged PSF and background images at each image pixel and normalize to the appropriate merged exposure maps to create final fluxed sensitivity images in each energy band (three per field; an example sensitivity image is shown in Figure 14).

We calculate empirical sensitivity curves in the SB, HB and FB for each of the four XDEEP2 fields using the sensitivity images derived above (see Figure 15). Due to the small overlapping regions in Fields 2–4, the sensitivity curves are found to be relatively smooth over the entire survey region with relatively sharp cut-offs at $f_{X,SB} \sim 4 \times 10^{-15}\,\mathrm{erg\,cm^{-2}\,s^{-1}}$, $f_{X,HB} \sim 9 \times 10^{-15}\,\mathrm{erg\,cm^{-2}\,s^{-1}}$ and $f_{X,FB} \sim 7 \times 10^{-15}\,\mathrm{erg\,cm^{-2}\,s^{-1}}$. Hence, the sensitivity limit is approximately uniform across the ma-
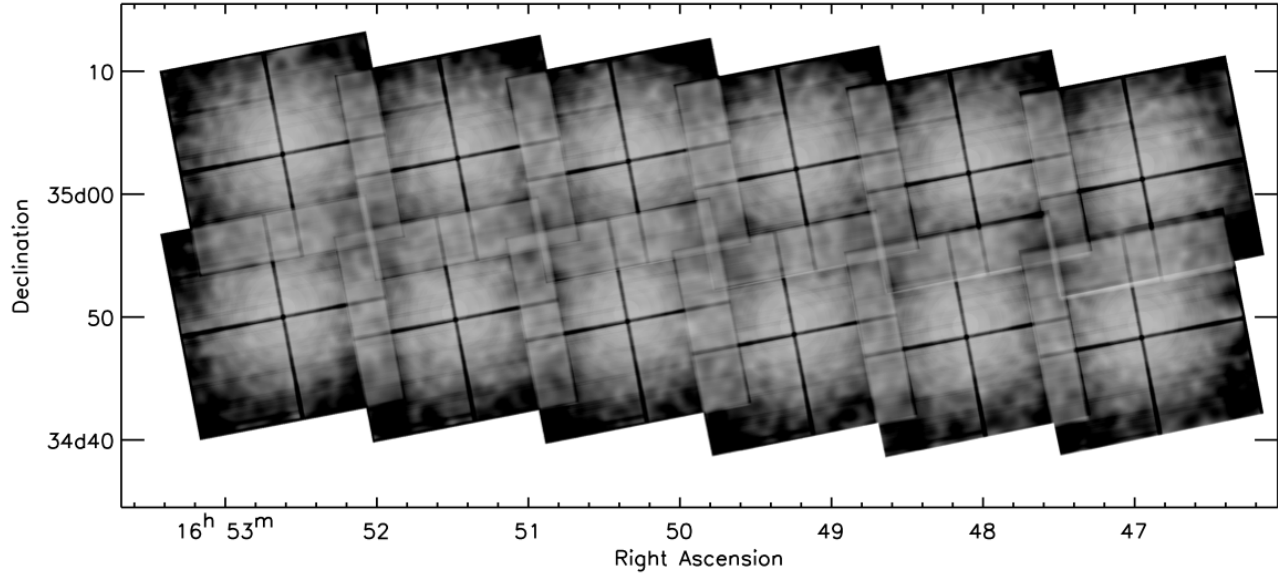
FIG. 14.— Example of an exposure-corrected full-band flux sensitivity map for an XDEEP2 field. The sensitivity map has been created as described in section 4.1. Areas with lightest (darkest) colors correspond to those regions of the map with the greatest (poorest) sensitivity.
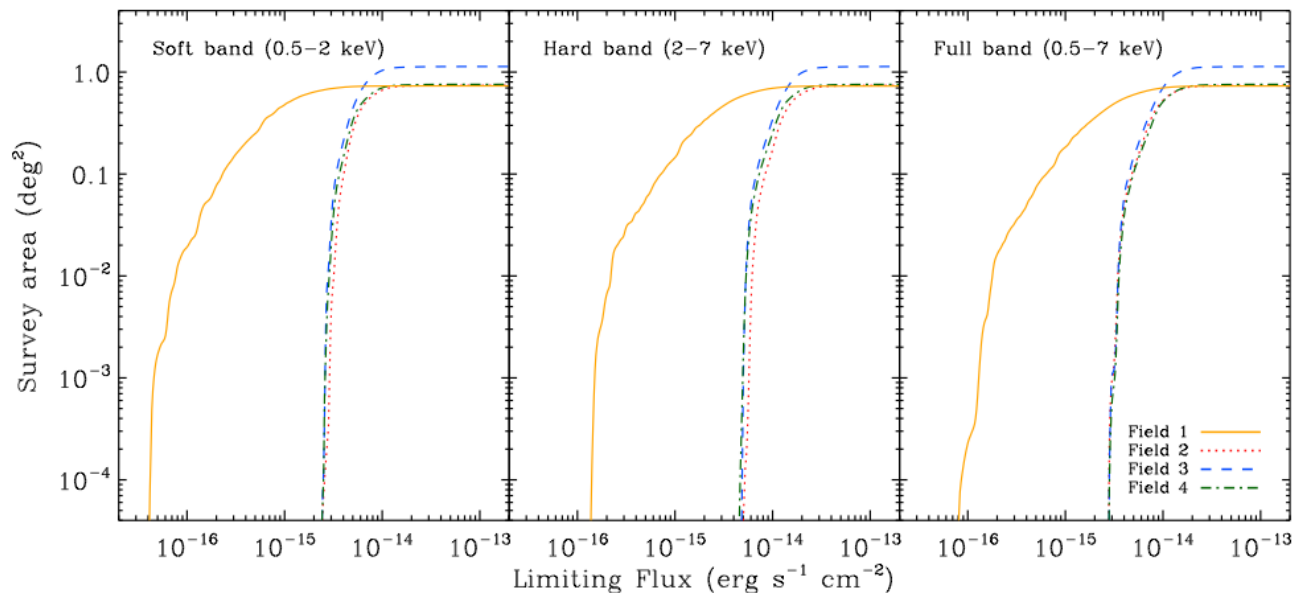

FIG. 15.— Survey solid angle as a function of the limiting flux in the soft-band, hard-band and full-band (left, center and right panels, respectively) for each XDEEP2 field. Limiting fluxes in the full-band where at least 10% of the survey field area are sensitive are $f_{X,1} > 2.8 \times 10^{-16}\,\mathrm{erg\,cm^{-2}\,s^{-1}}$, $f_{X,2} > 4.5 \times 10^{-15}\,\mathrm{erg\,cm^{-2}\,s^{-1}}$, $f_{X,3} > 4.6 \times 10^{-15}\,\mathrm{erg\,cm^{-2}\,s^{-1}}$ and $f_{X,4} > 4.6 \times 10^{-15}\,\mathrm{erg\,cm^{-2}\,s^{-1}}$.

jority of the survey area in Fields 2, 3 and 4. By contrast, the wedding-cake style observational setup of Field 1 combined with changing roll angles produces small (~ 0.1 deg^2) regions of high sensitivity, which combine over the field to produce a much more shallow sensitivity curve (i.e., the sensitivity is non-uniform). However, as the average exposure across Field 1 is ≈ 20–100 times greater than Fields 2–4, the mean sensitivity to the *detection* of faint sources is vastly improved in Field 1. We find that the limiting flux in the 0.5–7 keV band for source detection, which includes at least 10% of the survey area, is a factor ≈ 16 lower in Field 1 ($f_{X,FB} > 2.8 \times 10^{-16}\,\mathrm{erg\,cm^{-2}\,s^{-1}}$) than in Fields 2–4 ($f_{X,FB} > 4.5 \times$

$10^{-15}\,\mathrm{erg\,cm^{-2}\,s^{-1}}$, $f_{X,FB} > 4.6 \times 10^{-15}\,\mathrm{erg\,cm^{-2}\,s^{-1}}$ and $f_{X,FB} > 4.6 \times 10^{-15}\,\mathrm{erg\,cm^{-2}\,s^{-1}}$, respectively).

4.2. Comparison of X-ray sources in Field 1 to Laird et al. (2009)

As stated previously, while the analyses presented here include the recent 600ks observations of AEGIS 1–3, the 200ks X-ray source catalog for Field 1 (*AEGIS-X*) has been previously presented in Laird et al. (2009). Furthermore, the new 600ks observations will also be presented in a forthcoming paper (Nandra et al. in prep.) using similar detection and Bayesian-style sensitivity analyses to that used for the previous *AEGIS-*

TABLE 5
XDEEP2 SOURCE CATALOG

Nomenclature			Positional[d]			Radii[e]		D_OA[f]	Net Counts Soft[g]				Net Counts Hard[h]				Net Counts Full[i]				Flux[j]						Hardness Ratio[k]			Flux Ratio[l]		
DEEP2[a] Name	DEEP2[b] Field Name	CSC[c] Name	α_{J2000} (°)	δ_{J2000} (°)	Err (″)	R_{50} (″)	R_{90} (″)	(″)	50	50er	90	90er	50	50er	90	90er	50	50er	90	90er	S	S_er	H	H_er	F	F_er	HR	er_lo	er_up	FR	er_lo	er_up
									(counts)				(counts)				(counts)				(10^{-16} erg cm^{-2} s^{-1})											
aeg1_001	F1_AEG1	CXOJ141907.7+525946	214.78246	52.99710	0.84	4.48	10.36	632.0	16.62	5.77	31.17	8.86	23.17	7.15	48.97	12.25	39.81	8.74	80.26	14.70	3.18	1.44	16.02	5.62	19.2	3.78	0.20	0.04	0.43	4.75	3.18	7.66
aeg1_002	F1_AEG1	CXOJ141907.8+530025	214.78334	53.00712	0.32	4.45	10.30	628.4	162.4	13.99	311.9	19.55	57.06	9.42	95.73	13.98	219.1	16.46	406.0	23.62	50.6	3.21	40.6	6.48	91.2	6.14	-0.53	-0.59	-0.47	0.88	0.69	0.97
aeg1_003	F1_AEG1	-	214.79521	52.98033	1.18	6.91	12.42	611.5	14.31	-1	22.97	-1	35.58	-1	54.85	-1	50.6	-1	77.82	-1	-1	-1	25.1	6.30	18.3	4.09	0.53	0.30	0.84	12.37	7.12	-1
aeg1_004	F1_AEG1	CXOJ141911.2+530320	214.79699	53.05600	1.24	4.48	10.33	623.2	12.51	5.10	20.42	7.36	12.09	-1	23.29	-1	21.19	6.82	42.3	10.65	474.	91.2	824.	-1	1710	208.	-0.55	-1.00	-0.40	1.17	0.18	3.78
aeg1_005	F1_AEG1	CXOJ141919.9+530254	214.83506	53.04790	0.84	3.42	7.95	536.8	10.13	4.84	43.10	9.10	15.51	6.08	46.83	11.03	25.57	7.31	89.53	13.87	4.55	1.31	17.7	4.55	19.3	3.18	0.02	-0.11	0.20	3.26	2.25	4.34
aeg1_006	F1_AEG1	CXOJ141920.6+530028	214.83600	53.00792	0.29	3.03	7.11	514.7	117.3	12.04	226.4	16.77	12.68	-1	28.79	10.21	127.6	12.91	255.2	19.24	23.7	1.76	8.15	3.07	42.3	3.22	-0.79	-0.85	-0.70	0.41	0.25	0.56
aeg1_007	F1_AEG1	CXOJ141922.8+530132	214.84506	53.02555	0.21	2.86	6.75	498.7	100.1	11.24	161.1	14.59	121.0	12.44	222.9	17.61	221.2	16.32	384.7	22.44	18.4	1.66	73.1	5.75	70.0	4.07	0.16	0.10	0.21	4.05	3.54	4.44
aeg1_008	F1_AEG1	-	214.85376	52.99871	2.53	3.14	5.65	477.5	4.29	7.76	5.82	4.46	7.09	-1	13.20	-1	8.13	-1	19.02	-1	0.62	-1	0.59	-1	0.78	-1	-0.54	-1.00	-0.45	2865.	0.06	-1
aeg1_009	F1_AEG1	-	214.85694	53.00549	0.43	2.53	6.01	469.5	9.02	-1	16.26	-1	12.63	5.56	34.74	9.91	21.65	6.83	51.0	13.05	0.76	0.59	13.4	2.07	13.4	2.90	-0.03	-0.17	0.13	2.88	2.14	3.96
aeg1_010	F1_AEG1	-	214.85765	53.01971	0.96	2.53	6.06	469.6	20.15	5.88	42.87	8.77	27.37	6.90	41.56	10.01	47.39	8.60	83.7	12.87	0.88	0.78	9.82	2.90	9.82	-1	0.80	0.74	1.00	9117	18.87	-1
aeg1_011	F1_AEG1	-	214.86239	53.03122	0.54	2.56	5.98	464.7	22.14	6.08	44.39	8.83	11.39	-1	24.43	9.07	33.24	7.62	69.73	12.22	1.63	0.80	11.3	2.02	11.3	2.70	-0.06	-0.23	0.20	1.92	1.11	3.12
aeg1_012	F1_AEG1	-	214.86615	53.02515	0.56	2.44	5.75	453.7	10.17	4.71	29.25	7.81	18.13	6.08	27.73	9.26	28.58	7.23	58.53	11.67	0.88	0.91	9.24	1.86	9.24	2.67	-0.06	-0.23	0.20	3.14	1.96	4.95
aeg1_013	F1_AEG1	CXOJ141928.0+525840	214.86670	52.97822	0.25	2.42	5.70	461.1	76.61	9.93	149.7	13.82	37.22	7.62	58.93	10.64	113.9	12.08	208.9	17.02	15.9	1.47	18.0	3.26	35.5	2.89	-0.34	-0.51	-0.10	1.18	0.97	1.44
aeg1_014	F1_AEG1	-	214.87337	53.03977	0.29	2.37	5.63	448.2	52.24	8.47	87.44	11.22	29.69	7.07	59.41	10.85	81.87	10.58	146.5	15.17	8.73	1.13	16.8	3.15	23.2	2.44	-0.43	-0.51	-0.35	2.12	1.62	2.50
aeg1_015	F1_AEG1	-	214.87634	53.04383	1.07	3.21	5.78	446.2	13.05	5.34	22.20	7.27	4.52	-1	12.87	8.22	15.98	6.83	33.72	10.53	5.35	1.74	5.35	0.41	5.35	0.41	-0.19	-0.29	-0.09	0.24	0.09	0.64
aeg1_016	F1_AEG1	-	214.87842	53.00748	1.44	3.34	6.01	422.9	12.95	5.34	21.81	7.27	4.74	-1	7.56	-1	17.48	6.47	29.37	9.83	2.11	0.71	2.67	1.53	2.67	0.64	-0.36	-0.70	0.05	0.27	0.02	1.31
aeg1_017	F1_AEG1	CXOJ141930.8+525915	214.87886	52.98781	0.42	2.11	5.00	428.3	30.90	6.81	62.29	9.67	9.90	-1	18.33	-1	36.53	7.62	79.83	11.87	5.10	0.98	5.35	-1	13.0	-1	-0.81	-1.00	-0.78	0.86	0.53	1.58
aeg1_018	F1_AEG1	-	214.88704	53.04167	1.12	2.96	5.33	421.8	10.14	4.85	14.38	6.31	4.26	-1	6.75	-1	13.21	6.28	20.96	9.27	1.51	0.65	3.62	1.53	3.62	0.61	-0.61	-0.75	-0.43	0.78	0.16	4.05
aeg1_019	F1_AEG1	-	214.88706	52.99963	0.82	1.86	4.58	405.0	7.57	-1	12.61	-1	10.46	4.84	17.61	7.37	21.16	8.00	31.18	-1	1.23	-1	4.92	2.08	3.44	1.32	-0.43	-1.00	-0.23	7412.	6.61	-1
aeg1_020	F1_AEG1	-	214.88917	53.09005	1.37	4.92	8.88	496.5	20.36	6.37	24.09	8.12	16.40	-1	26.88	-1	31.18	8.00	31.18	-1	1.29	12.2	-1	3.20	7.86	-1	-0.71	-1.00	-0.64	2.09	0.16	6.51

NOTES—

[a] Unique source identifier

[b] XDEEP2 ObsID/sub-field name

[c] Unique source identifier for matched XDEEP2 sources present in the *Chandra* X-ray Source Catalog (CSC)

[d] X-ray position in J2000 co-ordinates (degrees) and associated centroid positional error (arc-seconds)

[e] Aperture radius in arc-seconds at 50% and 90% the effective area of ACIS-I given the off-axis distance of the X-ray source

[f] Off-axis distance in arc-seconds of X-ray source from aim-point of observation

[g] Soft-band (0.5–2 keV) net counts and associated errors in the R_{50} and R_{90} apertures

[h] Hard-band (2–7 keV) net counts and associated errors in the R_{50} and R_{90} apertures

[i] Full-band (0.5–7 keV) net counts and associated errors in the R_{50} and R_{90} apertures

[j] Total soft-band (S), hard-band (H) and full-band (F) fluxes and associated errors in units of 10^{-16} erg cm^{-2} s^{-1}

[k] Classical hardness ratios ($HR = (C_H - C_S)/(C_H + C_S)$) and associated 1σ upper and lower limits calculated using the BEHR method

[l] Flux ratios ($FR = F_{HB}/F_{SB}$) and associated 1σ upper and lower limits calculated using the BEHR method

X catalog. Since the source detection and extraction analyses differ significantly between *AEGIS-X* and the XDEEP2 catalog presented here, we now compare the detection methods and results.

Briefly, detection of sources in *AEGIS-X* was carried out using a custom implementation of the CIAO `wavdetect` tool. Laird et al. (2009) perform several runs of the detection software using different probability thresholds to build seed catalogs and to derive multiple estimates of the X-ray background in the observation. The final probability threshold for which a particular candidate is determined to be false in *AEGIS-X* is comparable to that used in our analyses. Laird et al. detected source candidates separately in the full, soft, hard and ultra-hard band images.[15] These source candidates were then combined into an individual source catalog using Bayesian techniques to statistically associate the source candidates and calculate the fluxes in the respective energy bands. The *AEGIS-X* catalog contains 1325 sources. Two sources (EGS4_258; EGS7_204, nomenclature adopted from Laird et al. 2009) in the *AEGIS-X* catalog were only detected in the ultra-hard band, i.e., an energy-band which we do not use due to the relatively small effective area of the telescope at these higher energies. Furthermore, four *AEGIS-X* sources (EGS4_240; EGS6_185; EGS7_194; EGS8_127) have 90% effective-area extraction regions which significantly ($> 50\%$) overlap with those extraction radii of other sources in the *AEGIS-X* catalog; from visual inspection we find that these four *AEGIS-X* sources (and their neighbors) are consistent with being single point sources. Hence, we remove these six sources from further comparison between the XDEEP2 and *AEGIS-X* catalogs.

We compared the 1319 unique source candidates identified in *AEGIS-X* to the 1720 source candidates identified in Field 1 of our XDEEP2 catalog solely on the basis of source position using the same varying matching radius method described in §5. We find that 1260 ($\approx 96\%$) of the source candidates identified in *AEGIS-X* are included in our new catalog. We have visually inspected each of the 59 *AEGIS-X* sources which were not identified in the XDEEP2 catalog. We find that the majority (44/59; $\sim 63\%$) of the *AEGIS-X* sources, which are not included as part of the XDEEP2 catalog, were detected by `wvdecomp` as source candidates in one energy band. However, on the basis of our MARX simulations, these 44 non-matched *AEGIS-X* sources did not meet our ultimate and more conservative count detection threshold and were removed as possibly spurious based on their low net counts ($C_{90,\mathrm{net}} \sim 5{-}10$). A further seven of the 59 non-matched sources were flagged as 'non-standard' and possibly spurious; we discuss these seven sources below. Finally, eight of the 59 non-matched *AEGIS-X* source candidates are not detected using `wvdecomp` after the inclusion of the more recent 600ks data.

We now briefly discuss the seven of the 59 non-matched *AEGIS-X* source candidates (EGS2_052; EGS5_105; EGS6_073; EGS6_093; EGS7_180; EGS8_093; EGS8_134) that were initially detected by `wvdecomp` and then highlighted by our routine as 'possibly spurious'. Visual inspection shows that three of these seven source candi-

dates, EGS6_093, EGS5_105 and EGS7_180) have their expected source PSFs partially blended with secondary brighter sources. Indeed, EGS6_093, is located between (< 2.5 arc-seconds) two significantly brighter X-ray sources (EGS6_164 and EGS6_165; both these sources are included in the *AEGIS-X* and XDEEP2 catalogs) causing sufficient detection ambiguity and EGS7_180 has an X-ray morphology consistent with that of a jet. These three sources, while initially detected in XDEEP2, are not included in our final catalog due to our inability to accurately separate the flux contribution from the neighboring bright source. Furthermore, EGS6_073 falls on a chip-gap; EGS2_052 has $C_{\mathrm{FB,net}} < 6$; and EGS8_134 has $\sim 50\%$ of its low source counts ($C_{\mathrm{FB,net}} \sim 7$) in one ACIS-I pixel, and is conservatively removed based on our MARX simulation analyses. Finally, EGS8_093 is possibly part of an extended source which appears extremely diffuse and only has a marginal detection ($P_{\mathrm{SB}} \sim 1.4 \times 10^{-6}$) in the *AEGIS-X* catalog.

As above, eight of the 59 non-matched *AEGIS-X* source candidates are not detected using `wvdecomp` after the inclusion of the 600ks data; while these sources were detected in the *AEGIS-X* analyses with $P_{\mathrm{band}} > 10^{-6}$, we note here that these sources may still be real, but are no longer detected due to intrinsic variability of the source. Similarly, Nandra et al. (in prep.) find that from a re-analysis of *AEGIS-X*, 17 of the *AEGIS-X* sources are no longer detected in the three sub-fields which include the new 600ks data. Assuming a similar number of non-detected source candidates across all of Field 1, this would suggest a false source contamination rate of ≈ 45 sources ($\approx 3.5\%$) in *AEGIS-X*.

In Figure 16 we show a comparison between the soft-band fluxes for isolated and formally-detected point-sources in the *AEGIS-X* (classically derived flux) and XDEEP2 catalogs. We have converted the fluxes we derived using $\Gamma = 1.7$ in XDEEP2 to $\Gamma = 1.4$, as used in *AEGIS-X*, using a conversion of 1.031 and we have corrected the *AEGIS-X* fluxes for galactic absorption (a factor of 1.042; Laird et al. 2009). We find excellent agreement between the fluxes derived in the XDEEP2 and *AEGIS-X* catalogs with a Spearman's rank coefficient of $r \sim 0.963$ which is significant at $P > 99.99\%$ level. Additionally, we have used two-dimensional linear-regression analyses to calculate the 3σ uncertainty on the derived correlation between the XDEEP2 and AEGIS-X source fluxes (dotted-lines in Figure 16), and the 3σ error region on the photon counts used to derive the source fluxes (dash-dot-lines in Figure 16). As expected, the Poissonian error due to low source counts significantly dominate the uncertainty towards low fluxes. We find that 12 ($\lesssim 0.1\%$) of the matched XDEEP2–*AEGIS-X* sources lie substantially outside the 3σ error region. These outlying sources have large numbers of counts ($\gg 100$) and/or are significantly extended beyond the expected 90% EEF angular size in the merged ACIS-I images. This suggests that these outlying sources are strong candidates for galaxy clusters and/or moderately variable quasi-stellar objects (QSOs).[16] Furthermore, variations in extraction radii at large offaxis distances, due to the introduction of the more recent ACIS-I observations (which

---

[15] In *AEGIS-X* the ultra-hard band is defined in the energy range 4–7 keV.

[16] As noted previously, the cluster candidates and their properties will be discussed in detail in a forthcoming publication.
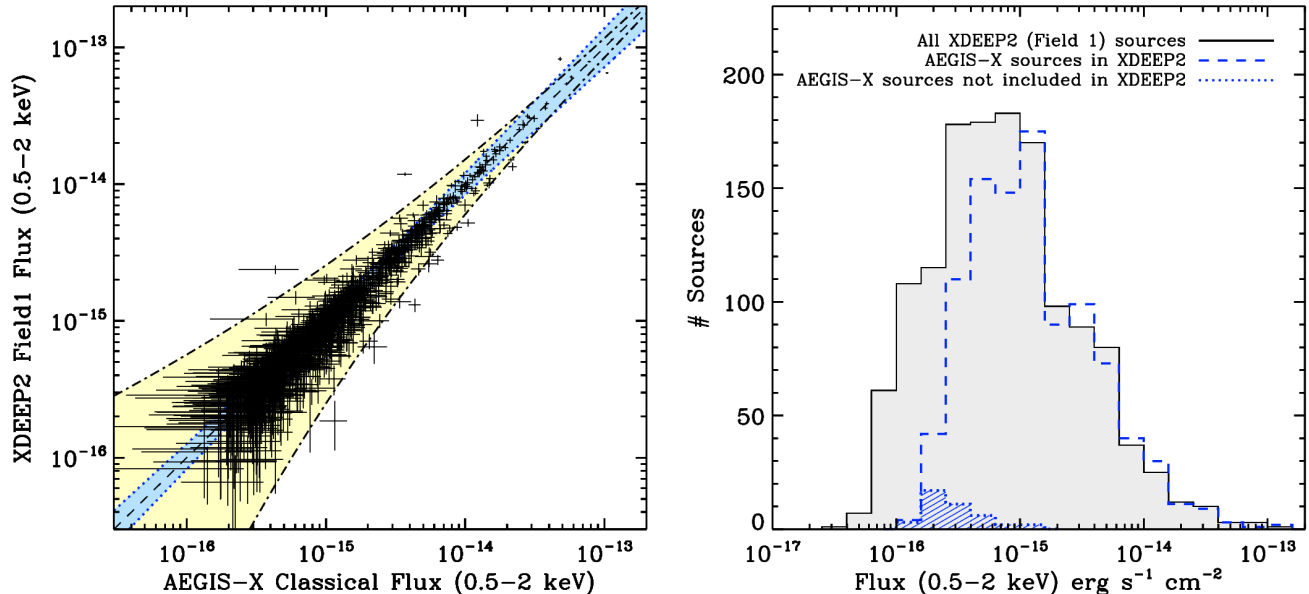
FIG. 16.— **a (left):** Comparison of X-ray source fluxes in the 0.5–2 keV energy band for the 1260 sources in common between the previous AEGIS-X source catalog and the XDEEP2 catalog presented here. The AEGIS-X sources are corrected for galactic absorption. The XDEEP2 fluxes are converted to $\Gamma = 1.4$ to match the AEGIS-X catalog. The dashed-line is the best-fit linear-bisector to the logarithms of the source fluxes. The blue-shaded region (dotted-lines) represents the 3σ uncertainty on the linear correlation calculated using 2-dimensional linear regression analyses. The yellow-shaded region (dash-dot-lines) represents the 3σ Poissonian error on the source fluxes due to photon-counting statistics, derived using the formalism of Gehrels (1986). We find a very strong agreement at the 99.99% level between XDEEP2 and AEGIS-X source fluxes. The $\lesssim 0.1\%$ of outliers are significantly extended in the ACIS-I images and/or have $\gg 100$ counts, suggesting that these sources are strong candidates for galaxy clusters and/or moderately variable QSOs. **b (right):** Soft-band source flux distributions (0.2 dex bin-width) for all X-ray sources detected in XDEEP2 (gray-shaded region) and AEGIS-X (blue-dash). The flux distribution of the 59 AEGIS-X source candidates which lack secure matches in XDEEP2 are highlighted with blue-hashed shading.

were performed with substantially different roll-angles) may potentially cause significant differences in measured counts/flux for bright X-ray sources with non-point-like profiles, such as galaxy clusters. Indeed, we find that when considering only the previous 200ks observations studied in Laird et al., with matched extraction apertures, the fluxes for all of the matched XDEEP2–*AEGIS-X* sources are consistent to within 1σ.

In Figure 16 we show the source flux distributions in *AEGIS-X* and XDEEP2 including the 460 new XDEEP2 sources which are detected in the new deeper 600 ks observations. As expected, the majority of these 460 new XDEEP2 sources have $f_{0.5-2\mathrm{keV}} \sim (8-80) \times 10^{-16}\,\mathrm{erg\,cm^{-2}\,s^{-1}}$, extending the distribution of the previous catalog to lower source fluxes. We additionally highlight the fluxes of the 59 *AEGIS-X* source candidates, which we conservatively do not include in XDEEP2. Each of these non-matched sources have $f_{0.5-2\mathrm{keV}} < 1.3 \times 10^{-15}\,\mathrm{erg\,cm^{-2}\,s^{-1}}$, with the vast majority at the extreme low-flux end of the main *AEGIS-X* source-flux distribution ($f_{0.5-2\mathrm{keV}} \sim (1-4) \times 10^{-16}\,\mathrm{erg\,cm^{-2}\,s^{-1}}$). Using a Bayesian counterpart matching algorithm, which we present in § 5, we have attempted to assign DEEP2 optical counterparts to the 59 *AEGIS-X* source candidates. We find that the majority (35/59; $\sim 60\%$) of these *AEGIS-X* source candidates lack secure optical counterparts; this is a factor ~ 2 larger than the fraction of X-ray sources which lack counterparts across the entire XDEEP2 sample ($\sim 29\%$). However, based on simulations of a purely random set of 59 source positions, we would expect only $\sim 3-7$ spurious counterpart matches using our Bayesian matching algo-

rithm. Hence, the 24 *AEGIS-X* sources found to coincide with an optical counterpart is a factor $\sim 3-8$ larger than the random expectation of spurious counterparts, suggesting that some of these X-ray sources may be real.

Based on our rigorous comparison of the *AEGIS-X* catalog and our XDEEP2 catalog, we suggest that the two catalogs appear to be in excellent agreement, despite the use of different detection algorithms (`wavdetect` versus `wvdecomp`). In general, the small ($\approx 4\%$) discrepancy between the catalogs can be attributed to the removal of low significance sources in the XDEEP2 catalog based on our MARX simulations. Additionally, we stress that since 51 of the 59 low significance sources are initially identified by both `wavdetect` and `wvdecomp`, we cannot rule out that they are real sources, although they ultimately did not meet our more conservative detection criteria.

4.3. Comparison of X-ray sources in Fields 2–4 to the Chandra Source Catalog

The Chandra Source Catalog (CSC) is a compilation of all relatively bright X-ray sources detected in single ACIS and HRC imaging observations by the Chandra X-ray Observatory in the first eight years of the mission (Evans et al. 2010). In principle, the X-ray sources detected in XDEEP2 Fields 2–4 and by the CSC are likely to be equivalent. Similar to the CSC, we have not attempted to merge events in overlapping regions of Fields 2–4 as, in general, these regions occur at large off-axis distances where the *Chandra* PSF is poor. In this section, we compare the XDEEP2 source properties to those detected in the CSC release 1.1. The current CSC
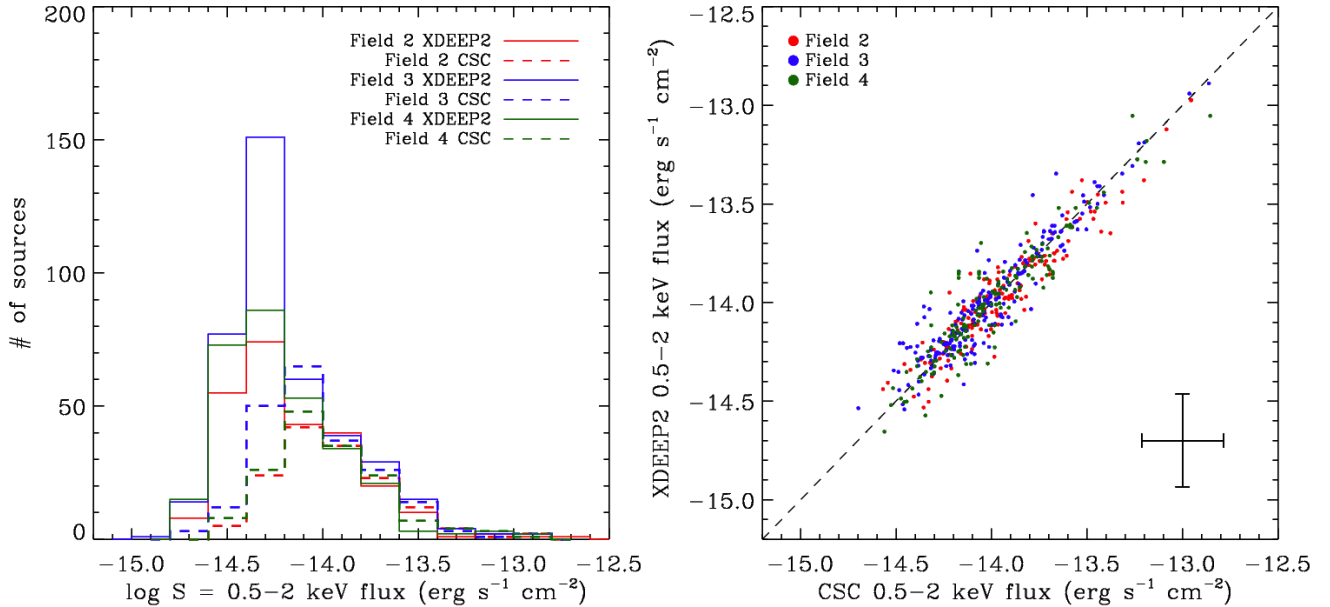
FIG. 17.— **a (left):** Soft-band (0.5–2 keV) flux distributions for all X-ray sources identified in the *Chandra* ACIS-I observations of XDEEP2 Fields 2 (red), 3 (blue) and 4 (green) within the XDEEP2 (solid lines) and CSC (dashed-lines) catalogs. **b (right):** Comparison of 0.5–2 keV fluxes for all XDEEP2 sources associated with CSC sources in Fields 2 (red dots), 3 (blue dots) and 4 (green dots). Error bar represents the median uncertainty in the flux estimates for the CSC and XDEEP2 sources.

data release contains X-ray data products and information (positions; spatial; temporal multi-band count rates; fluxes) for distinct point sources and compact sources, with observed spatial extents $\lesssim 30$" observed in publicly released data to the end of 2009. Highly extended sources, and sources located in selected fields containing bright, highly extended sources are excluded in the CSC. See http://cxc.cfa.harvard.edu/csc/index.html for further information.

We have used the publicly available java-applet, CSCview to associate the XDEEP2 X-ray sources in Fields 2–4 to the CSC Master Catalog. Although we do not attempt to merge the individual ACIS-I observations in Fields 2–4, we find that only $\sim 41.9 \pm 2.2\%$ (i.e., 150/342; 218/528; 158/386 sources in Fields 2, 3 and 4, respectively) of the XDEEP2 sources are identified in the CSC. In Figure 17a we show a comparison of the flux distributions for all XDEEP2 sources and CSC sources within the area covered by Fields 2, 3 and 4 of XDEEP2. The 90% EEF aperture fluxes produced by the CSC are derived using a simple absorbed powerlaw with $\Gamma = 1.7$ and $N_{\rm H} = 3 \times 10^{20} \, {\rm cm}^{-2}$. Hence, for the purposes of comparison we convert the field-specific $N_{\rm H}$ used to derive the XDEEP2 fluxes to match the CSC fluxes.

We find that while all CSC sources with $f_{0.5-2} \gtrsim 6 \times 10^{-15} \, {\rm erg \, cm}^{-2} \, {\rm s}^{-1}$ are identified in the XDEEP2 catalog, the vast majority of the lower flux XDEEP2 sources are not included in the CSC. By design, the detected CSC X-ray sources have $C_{\rm net} \gtrsim 10$ counts for an on-axis source ($\gtrsim 20$–30 counts for an off-axis source), i.e., the CSC catalog only includes sources whose flux estimates are greater than three times their estimated 1σ uncertainties. However, as we have shown in Figures 11 and 12, and has been shown conclusively by many other deep and wide-field X-ray surveys (e.g., CDF-N; CDF-S; C-COSMOS; AEGIS-X; XBootes), many X-ray sources

can be significantly identified with only ~ 3–5 net counts, although the source flux will remain relatively unconstrained due to Poisson uncertainties. Indeed, $\gtrsim 98\%$ of the XDEEP2 sources not identified in the CSC catalog have $C_{\rm net} < 20$ counts. Furthermore, to within 1σ, we find excellent agreement for the X-ray fluxes of the sources in common between XDEEP2 and the CSC (see Figure 17b).

Given that all of the CSC sources within the survey area are identified in the XDEEP2 catalog and the non-matched sources have lower counts/flux which lie above the thresholds derived from our extensive simulation analyses, we find that the CSC provides a more conservative identification of X-ray sources within the XDEEP2 fields. For completeness, we have also associated the X-ray sources identified in Field 1 to the CSC catalog, and find there are 689 distinct X-ray sources in common between the catalogs. The faintest CSC sources in Field 1 have $f_{0.5-2} \gtrsim 5 \times 10^{-16} \, {\rm erg \, cm}^{-2} \, {\rm s}^{-1}$, but with the majority at $f_{0.5-2} \gtrsim 2 \times 10^{-15} \, {\rm erg \, cm}^{-2} \, {\rm s}^{-1}$ (i.e., an average factor ~ 3 more sensitive per individual observation than Fields 2–4). For ease of comparison with future surveys, we include the CSC source identifiers as part of the XDEEP2 catalog, for all XDEEP2 sources with CSC counterparts.

4.4. *Source spectral properties: hardness ratios*

Using the Bayesian Estimator of Hardness Ratio (BEHR) method (Park et al. 2006), hardness count ratios (HR), defined as $HR = (C_{\rm HB} - C_{\rm SB})/(C_{\rm HB} + C_{\rm SB})$, where $C_{\rm SB}$ and $C_{\rm HB}$ are the counts in the soft and hard bands respectively, as well as the hardness flux ratios (FR), defined as $FR = F_{\rm HB}/F_{\rm SB}$, were calculated for all detected sources in the XDEEP2 catalog. FR and HR and their associated uncertainties calculated using BEHR are available in the main XDEEP2 source table. Briefly, BEHR treats the detected source and background X-ray

photons as independent Poisson random variables, and uses a Monte Carlo based Gibbs sampler to select samples from posterior probability count distributions to correctly propagate the non-Gaussian uncertainties, which derive from the calculation of hardness ratios. BEHR is particularly powerful in the low-count Poisson regime, and computes a realistic uncertainty for the HR and FR, regardless of whether the X-ray source is detected in both energy bands. In Table 5, we include the FR and HR ratios with the associated 1σ upper and lower limits for all XDEEP2 sources. Sources with unconstrained upper or lower limits due to non-detections are denoted by "-1" in the appropriate uncertainty column.

In Figure 18 we show the FR distribution for the XDEEP2 sources. Typically, the XDEEP2 sources which are detected in both the hard and soft-bands have FR in the range ~ 0.7–7, with distribution tails at low and high values of FR. Following previous studies (e.g., Bauer et al. 2002; Alexander et al. 2003a; Luo et al. 2008), we divide the X-ray sources with low and high-flux at $f_{\rm FB} \sim 4 \times 10^{-15}\,{\rm erg\,cm^{-2}\,s^{-1}}$ (i.e., the 10% flux limit of the shallow exposure XDEEP2 fields). While the choice of cut is somewhat arbitrary, clearly we find the same general trend towards higher values of FR for X-ray sources with low-fluxes as has been observed previously (e.g.,Hasinger et al. 1993; Vikhlinin et al. 1995; Giacconi et al. 2002; Tozzi et al. 2006). We find that the distribution of FR values is moderately peaked at FR ~ 1.3 sources with high flux ($f_{\rm FB} \gtrsim 4 \times 10^{-15}\,{\rm erg\,cm^{-2}\,s^{-1}}$). By contrast, lower flux sources have a more extended distribution, with a median value of FR ~ 2.1 and tailing to higher values of FR. Using the CIAO spectral analysis package, `sherpa`, we have simulated X-ray spectra for AGN populations at $0 < z < 6$ in order to quantify the evolution of X-ray spectral slopes due to the k-correction of the observed AGN spectra towards high-z. Based on these simulations, we find that the two peaks observed in the FR distributions are co-incident with the spectral slopes expected for two separate AGN populations with $\Gamma \sim 1.2$–1.4 and $\Gamma \sim 1.7$–1.8. Further, we find that the majority of the 460 low-flux sources in Field 1, which were not previously identified in AEGIS-X due to insufficient survey depth (see § 4.2), have a similarly wide FR distribution (~ 0.8–10) to the AEGIS-X source candidates and the sources identified in Fields 2–4. However, the median FR for the new faint Field 1 sources is shifted slightly higher with FR$\sim$3 (i.e., harder spectral indices), suggesting that these new sources have flatter X-ray spectral slopes, and are likely to be more heavily obscured. Hence, their previous non-detection in the 200ks data is due to the combined result of AGN luminosity, distance and intrinsic obscuration.

4.5. *XDEEP2 source number counts*

We have calculated the cumulative number of sources in the XDEEP2 catalog ($N(> S)$) detected per square degree that are brighter than a given flux in the soft (0.5–2 keV) band, i.e., the $\log N - \log S$ distribution (see Figure 19). This provides a good check that the merging of the datasets and the extensive calibrations were performed correctly, as well as an excellent comparison to previous X-ray surveys. We choose to compare in the soft-band as this is the most sensitive energy and the specific energy range definition of the soft-band (0.5–
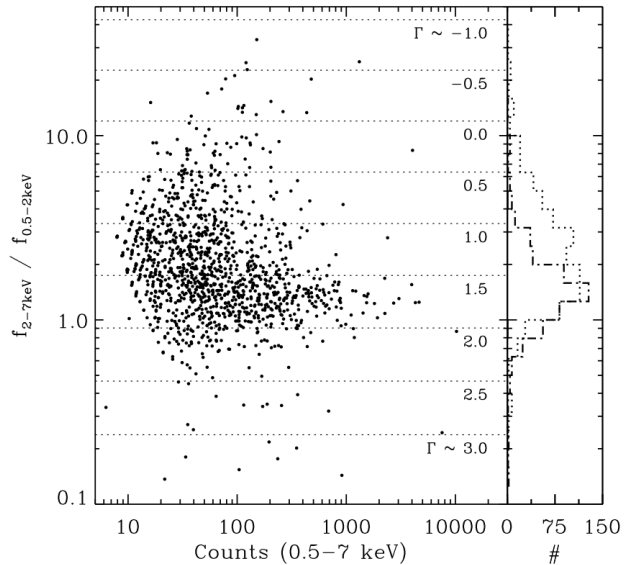

FIG. 18.— **Main panel:** Flux band ratio defined as FR = $f_{2-7{\rm keV}}/f_{0.5-2{\rm keV}}$ as a function of full-band counts ($C_{0.5-7keV}$) for all XDEEP2 sources detected in the soft and hard energy bands. Average spectral slopes for fixed values of FR established from X-ray spectral simulations using `Sherpa` are highlighted with horizontal dotted lines. **Right panel:** FR distributions for all detected sources within XDEEP2 with $f_{0.5-7{\rm keV}} \gtrsim 4 \times 10^{-15}\,{\rm erg\,cm^{-2}\,s^{-1}}$ (dot-dashed) and $f_{0.5-7{\rm keV}} \lesssim 4 \times 10^{-15}\,{\rm erg\,cm^{-2}\,s^{-1}}$ (dotted).

2 keV) is consistent across previous surveys. As a consequence of (1) the changing slope of the $\log N - \log S$ distribution towards fainter fluxes, and (2) observationally fainter sources possibly being more obscured and/or lower accretion rate AGN than brighter sources, the so-called 'Eddington bias' introduces many statistically low-significance sources at the sensitivity limit of the X-ray survey. Hence, we have empirically restricted our analyses presented in this section to only those sources detected with $f_{\rm SB} > 4.5\sigma_{\rm bkg,field}$, i.e., on-axis 0.5–2 keV fluxes of $f_X \gtrsim 9 \times 10^{-17}\,{\rm erg\,cm^{-2}\,s^{-1}}$ in Field 1 and $f_X \gtrsim 4 \times 10^{-15}\,{\rm erg\,cm^{-2}\,s^{-1}}$ in Fields 2–4 (equivalent to $C_{\rm SB,net} > 10$ and $C_{\rm SB,net} > 6$, respectively). For the purpose of comparison, we have converted all source and field fluxes to $\Gamma = 1.4$ and use the combined flux limits (see §4.1) to construct the $\log N - \log S$ distribution.

To quantify the uncertainties on the derived $\log N - \log S$, we have used a Monte-Carlo (MC) style simulation. Using the formal 1σ error on the source flux, we built symmetrical probability flux distributions ($P(f_X)$) for each source to be input to 10,000 realizations of our simulation. Within the MC simulation, we randomly assign fluxes to each source within the sample based on the individual $P(f_X)$, and recompute the $\log N - \log S$ distribution. The total 90% uncertainty on the $\log N - \log S$ is then defined as the mean absolute deviation of the 10,000 simulated distributions combined in quadrature with the 90% Poissonian error on the main distribution, defined using the formalism of Gehrels (1986). From our MC simulations, in Figure 19 we show that the XDEEP2 $\log N - \log S$ is very well constrained (~ 0.12 dex) in the flux range $f_X \sim (0.2$–5$) \times 10^{-15}\,{\rm erg\,cm^{-2}\,s^{-1}}$ owing to the large sensitive area in Field 1 around the 'knee' of the $\log N - \log S$ at $f_X \sim (6$–8$) \times 10^{-15}\,{\rm erg\,cm^{-2}\,s^{-1}}$.
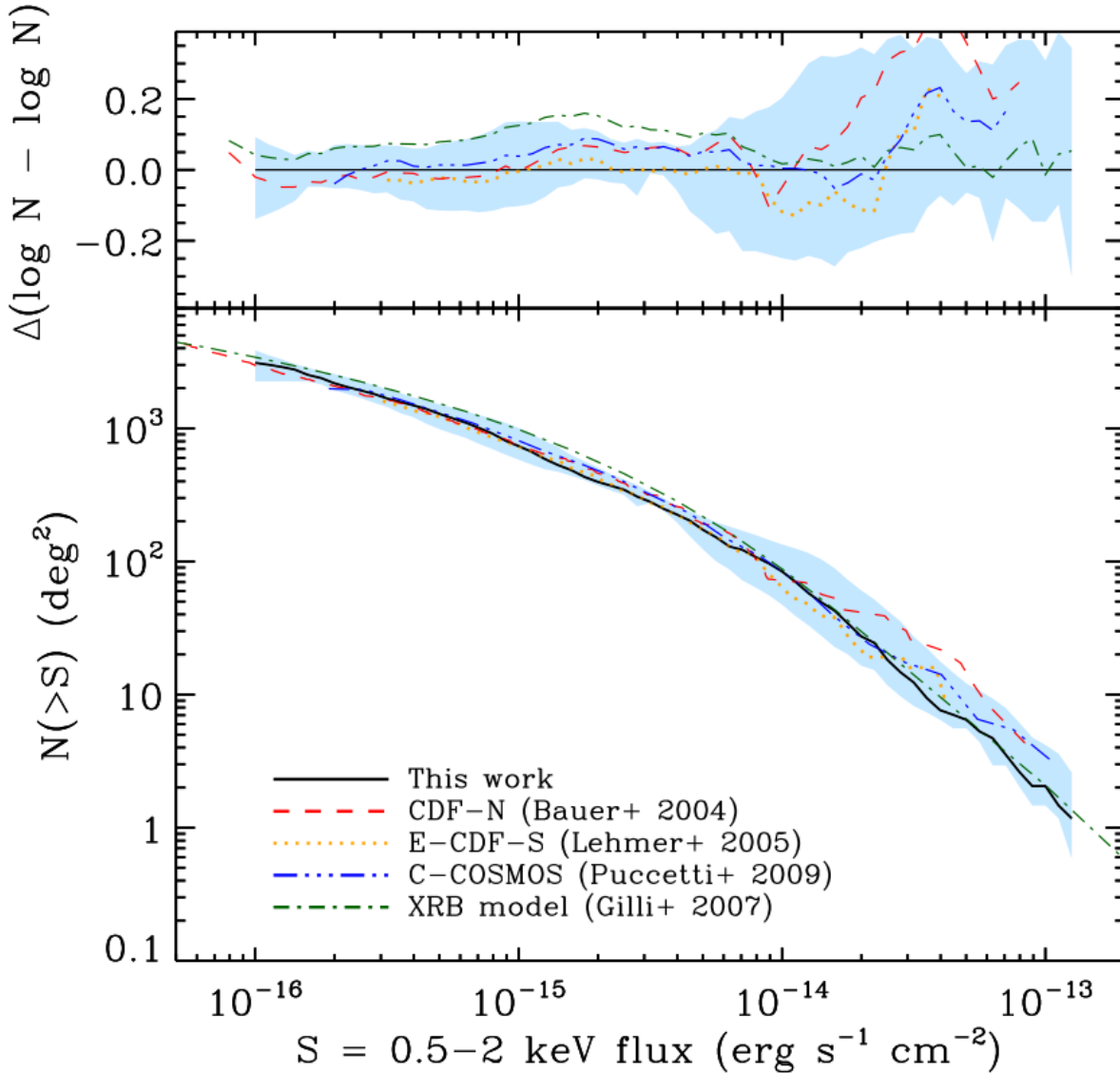
Fig. 19.— **Main panel:** Logarithm of the number of detected sources within the XDEEP2 catalog brighter than a given soft-band flux ($N(> S)$; black solid line) versus the logarithm of soft-band flux (i.e., the $\log N$–$\log S$ distribution). For comparison to previous surveys, source fluxes were converted using $\Gamma = 1.4$. We use a Monte-Carlo simulation to assess the 90% uncertainty on the XDEEP2 distribution due to flux errors and Poisson counting statistics (shaded region). We compare this $N(> S)$ distribution to previous surveys fields [CDF-N (Bauer et al. 2004); Extended-CDF-S (Lehmer et al. 2005); *Chandra*-COSMOS (Puccetti et al. 2009)] and to an X-ray background synthesis model (Gilli et al. 2007). **Top panel:** Logarithm of the residuals between $N(> S)$ XDEEP2 and the comparison $N(> S)$ curves. The logarithm of the uncertainty for the $\log N$–$\log S$ is shown by the shaded region. We find good agreement ($< 10\%$ deviation) between XDEEP2 and all previous observation surveys in the regime $f_X < 1 \times 10^{-14} \, \mathrm{erg} \, \mathrm{cm}^{-2} \, \mathrm{s}^{-1}$. However, we show a mild systematic offset towards lower N for sources with $f_X > 2 \times 10^{-14} \, \mathrm{erg} \, \mathrm{cm}^{-2} \, \mathrm{s}^{-1}$, in closer agreement with XRB models.

However, we find that the uncertainty on the distribution increases to ~ 0.3 dex towards the bright flux tail ($f_X \gtrsim 10^{-14} \, \mathrm{erg} \, \mathrm{cm}^{-2} \, \mathrm{s}^{-1}$) of the $\log N$–$\log S$. We determined that this is caused by the decrease in the space-density of the far rarer bright sources, combined with the relatively large uncertainties on the fluxes for those sources identified in the more shallow exposure Fields 2–4. For these particular sources, which dominate the distribution within this moderate–high flux regime, the majority are detected with relatively few counts (~ 6–15) and hence, 1σ flux errors are ~ 25–50% of the overall flux. In turn, these relatively large flux uncertainties cause significant scatter of the sources within the simulated distributions.

In Figure 19, we additionally compare the $\log N$–$\log S$ derived from XDEEP2 to the distributions found in previous wide and deep *Chandra* surveys [CDF-N (Bauer et al. 2004); Extended-CDF-S (Lehmer et al. 2005); *Chandra*-COSMOS (Puccetti et al. 2009)]. In the flux range $f_X \sim (0.09$–$20) \times 10^{-15} \, \mathrm{erg} \, \mathrm{cm}^{-2} \, \mathrm{s}^{-1}$, we find excellent agreement with these previous surveys. We confirm previous results (e.g., Luo et al. 2008), that the CDF-N field may be subject to mild cosmic variance, as it appears to over-estimate (a factor ~ 1.5–4) the number count distribution of sources with $f_X \gtrsim 10^{-14} \, \mathrm{erg} \, \mathrm{cm}^{-2} \, \mathrm{s}^{-1}$. Furthermore, using the X-ray back-

ground (XRB) synthesis models of Gilli et al. (2007), we have simulated the expected $\log N - \log S$ distribution of both obscured and unobscured populations of AGN with $N_H \sim 10^{20}$–10^{25} cm^{-2}, $L_X \sim 10^{38}$–10^{46} L$_\odot$ in the redshift range $z \sim 0$–8. In accordance with previous surveys, we consistently underestimate the number counts of AGN with $f_X \lesssim 8 \times 10^{-15}$ erg cm^{-2} s^{-1} in comparison to that expected from the XRB (see upper panel of Figure 19), suggesting that many heavily obscured sources are still being missed in even the most sensitive surveys. Indeed, multi-wavelength studies of deep and wide field X-ray surveys find a large population of seemingly obscured AGN which remain undetected using X-ray data alone (e.g., Alonso-Herrero et al. 2006; Donley et al. 2007; Daddi et al. 2007; Meléndez et al. 2008; Fiore et al. 2009; Brusa et al. 2010; Goulding et al. 2011; Georgantopoulos et al. 2011; Alexander et al. 2011). However, for XDEEP2 sources with $f_X \gtrsim 2.5 \times 10^{-14}$ erg cm^{-2} s^{-1}, we find a mild (≈ 30–50%) systematic offset from previous X-ray surveys (e.g., E-CDFS; C-COSMOS), resulting in number counts closer to those predicted by XRB models, although the results from each of these surveys are all consistent at the 90% significance level.

5. OPTICAL DEEP2 & X-RAY XDEEP2 SOURCE IDENTIFICATION

By design, the XDEEP2 *Chandra* survey is within the same spatial region as the DEEP2 Galaxy Spectroscopic Redshift survey fields. In this section we identify optical counterparts to the sources in the XDEEP2 catalog using a custom Bayesian style analysis. For DEEP2, optical B, R and I-band photometry was obtained with the Canada-France-Hawaii Telescope (CFHT) 12k camera. The main photometric catalog contains over $> 710,000$ sources with a typical absolute astrometric accuracy of ~ 0.2 arc-seconds and is complete to $R_{\rm AB} \sim 25.2$ (see Coil et al. 2004). In Table 6 we show the breakdown for the approximate number of optical sources within the XDEEP2 survey fields. In DEEP2 Field 1, all galaxies which have magnitudes of $R_{\rm AB} < 24.1$ were targeted for spectroscopy using the DEIMOS spectrograph on Keck (see Davis et al. 2003 for further information on the observational setup of DEEP2). However in Fields 2–4, only those galaxies which meet both a simple BRI color-cut threshold and have magnitudes of $R_{\rm AB} < 24.1$ were targeted. The 4th data release of the DEEP2 spectroscopic catalog contains 50,319 unique sources (Newman et al. 2012).

5.1. A Bayesian optical–X-ray matching routine

Given the unique observational construction of the combined XDEEP2 survey, in that it is both relatively shallow in wide areas, while simultaneously being extremely deep in smaller regions across the fields, we require a method of source matching which will account for changes in both the optical and X-ray source densities and statistically associate bright X-ray sources in the shallow fields with optical counterparts which are likely to contain bright AGN (i.e., QSOs). To this end, we have extended the Bayesian source-matching algorithm of Brand et al. (2006) to now include the X-ray source density and the properties of the candidate optical counterparts. Briefly, this method uses Bayesian-style statistics to calculate the probability of a random association
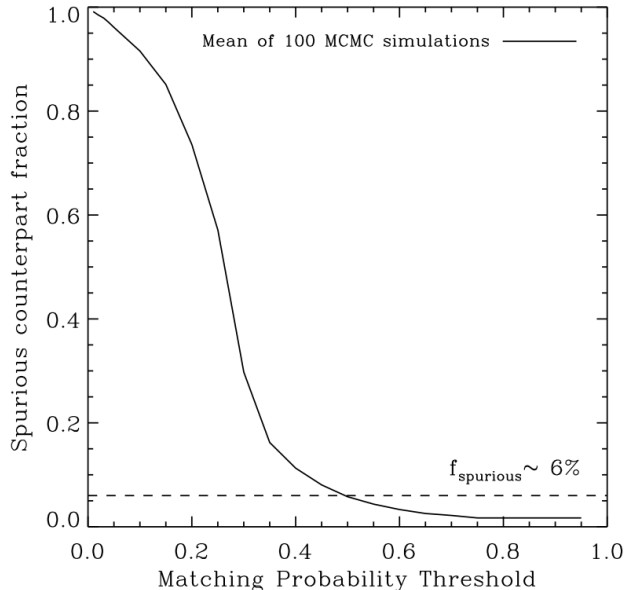

FIG. 20.— Fraction of counterparts found between the DEEP2 optical catalog and 100 randomly simulated X-ray catalogs. We find that the fraction of spurious matches decreases rapidly as a function of the probability threshold (P(match)) calculated in our Bayesian-style matching algorithm. For P(match) = 0.46, we expect a spurious matching fraction of $\lesssim 6\%$ (dashed-line).

occurring between two counterparts given the angular and magnitude distributions of the optical sources in a specific region of the sky. Simultaneously this algorithm accounts for the distribution of matching radii appropriate for a given off-axis position of the X-ray source in a *Chandra* observation. Furthermore, we allow modifications to the optical source positions, assuming a Gaussian probability based on the centroid and astrometric error of the DEEP2 data. As stated previously, median offsets between DEEP2 and XDEEP2 have been removed a-priori (see § 2.4). We use a Gaussian prior based on the characteristics of the *Chandra* PSF for the positional uncertainty of the X-ray source to derive the probability, f of an X-ray source having an optical counterpart within the catalog (i.e., the survey mean completeness). We combine these posterior assumptions with information specific to the X-ray source (total counts, background level, proximity to other X-ray sources) and the optical properties (star, normal galaxy, quasar etc.) of possible counterparts to assign likelihood association probabilities between pairs of sources. In our new implementation of the algorithm, the probability of identifying an X-ray source i with optical source k is then,

$$P_{ik,match} = f \frac{M_{ik}}{B_k} F_{ik} O_{ik} \left[(1-f) + f \sum_{l=1}^{n_i} \sum_{k=1}^{n_j} \frac{M_{il}}{B_l} F_{jk} \right]^{-1}$$
(3)

where M_{ik} is the simple Gaussian probability of associating an X-ray source i with an optical counterpart k at a given separation including the X-ray and optical positional uncertainties; B_k are the Poisson-idealized number counts as a function of optical magnitude within a region encompassing the X-ray position, in effect, B_k accounts for both the changing R-band magnitude depth
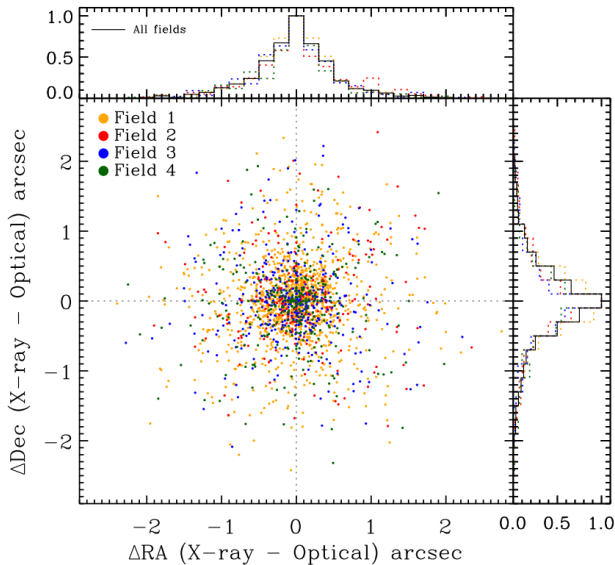
FIG. 21.— Positional offset between optical and X-ray positions for the 2126 XDEEP2 X-ray sources with secure DEEP2 optical counterparts found using our Bayesian-style matching algorithm. The spread in residuals is approximately Gaussian across all four DEEP2 fields with a mean positional offset of $\Delta_{\alpha,\delta} < 0.45$ arc-seconds between the X-ray and optical source catalogs.

and source density within the optical DEEP2 catalog; F_{ik} is the probability that an X-ray source of a given flux and flux limit has an optical association which is then marginalized over the R-band magnitude of the proposed optical counterpart; and O_{ik} is the probability function containing the optical classification of the source, and is essentially a weighting based on the probabilistic galaxy classification of the source ($P(gal)$ of 0 (=star) to 1 (=galaxy) defined in Coil et al. 2004) derived from the optical photometry and SED fitting. We determine the priors for F_{ik} by randomly selecting from a cumulatively summed set of Poisson distributions in Markov-Chain simulations of the X-ray and optical catalogs. For computation speed, we limit the counterpart selection to only optical sources detected in the R-band. This also conforms with the selection method used to determine targets for optical spectroscopy. We note here, that while this method increases our ability to include optical sources with R-band magnitudes fainter than the completeness limit of the DEEP2 survey ($R \sim 25.2$ mags), the identification of X-ray sources with optically-faint counterparts is still incomplete at $R \gtrsim 25.2$ (e.g., Alexander et al. 2001; Brusa et al. 2010).

To compute the probability threshold required to accept the optical source as a counterpart to the X-ray source and to quantitatively assess the false association fraction, we simulated mock XDEEP2 catalogs and compared them to the optical DEEP2 catalog. Following Brand et al. (2006), we randomized the positions of the XDEEP2 sources by $\pm 30''$ offsets and compared the number of false matches produced. In Figure 20 we show the behaviour of the fraction of spurious counterparts for a given matching probability threshold (P_{match}) produced by our association routine. We find that using $P_{\mathrm{match}} = 0.46$ produces one spurious optical counterpart for $\lesssim 6\%$ of the X-ray sources in the randomized

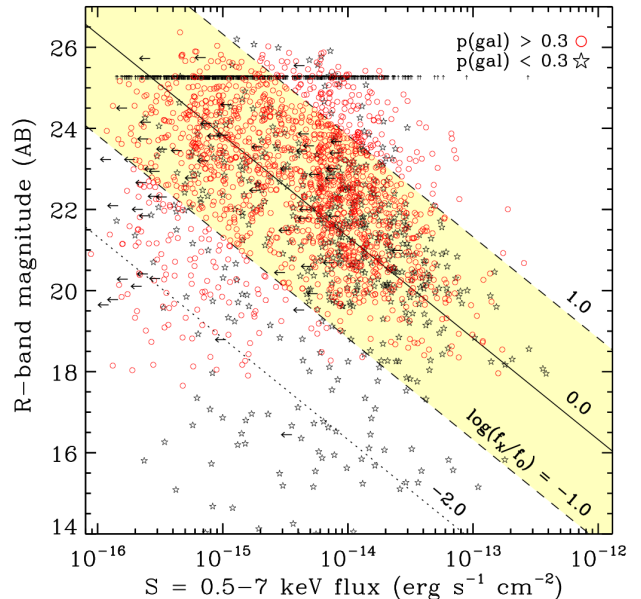FIG. 22.— R-band (AB) magnitude versus full-band (0.5–7.0 keV) flux for all XDEEP2 sources. X-ray sources are divided between those with galaxy probabilities ($P(gal)$) > 0.3 (i.e., optically extended sources; open circles) and < 0.3 (i.e., point-like sources; open stars). X-ray sources which lack optical counterparts are shown with upper-limits at $R = 25.2$, i.e., the magnitude-limit of the DEEP2 catalog. Additionally, constant X-ray–optical flux ratios (f_X/f_O) are shown for $\log(f_X/f_O) = \{-2.0; -1.0; 0.0; 1.0\}$, calculated using the relation of McHardy et al. (2003).

catalogs (see Figure 20). The spurious counterpart fraction of $\lesssim 6\%$ is chosen specifically to be consistent with that found for the previous *AEGIS-X* catalog which was matched using the Maximum Likelihood technique (see Civano et al. 2012, and references there-in); in turn, this also allows for further comparison between the catalogs. In 100 Markov-Chain Monte-Carlo (MCMC) simulations, we find that the spurious fraction remains relatively constant for $P_{\mathrm{match}} > 0.46$ across all four XDEEP2 fields with an overall dispersion of $< 1\%$ within the MCMC simulations.

In Figure 21 we present the offset in astrometric coordinates between the X-ray source position and that of the optical counterpart from the XDEEP2 catalog. We find that the spread in positional offsets is approximately Gaussian across all four DEEP2 fields with a mean positional offset of $\Delta_{\alpha,\delta} < 0.45$ arc-seconds with an approximately zero systematic offset between the two catalogs. This mean offset is consistent with that found in previous deep-wide surveys (e.g., C-COSMOS with 0.81" for 90% of the sources; Elvis et al. 2009; Civano et al. 2012) Furthermore, we find that the positional offset between the X-ray source and optical counterpart appears to be a moderately-strong function of the ACIS-I off-axis position with on-axis ($< 1.5'$) and off-axis ($> 6'$) X-ray sources having median offsets of $\sim 0.28''$ and $\sim 0.96''$, respectively.

5.2. *X-ray–optical source properties*

Of the 2976 X-ray sources in XDEEP2, we find that 2126 ($\approx 71.4 \pm 2.8\%$) have at least one secure optical counterpart in the DEEP2 optical catalog. Multiple candidate counterparts are found for $\approx 11\%$ of the X-ray

TABLE 6
X-RAY SOURCES WITH OPTICAL COUNTERPARTS

Field #[a]	$N_{\mathrm{X-ray,XDEEP2}}$[b]	$N_{\mathrm{opt,DEEP2}}$[c]	$N_{\mathrm{X-ray,opt}}$[d]	$f_{\mathrm{X-ray,opt}}$[e]	Median Δ_{RA}[f]	Median Δ_{Dec}[f]
1	1720	$\sim 100,200$	1183	68.8	-0.02	0.01
2	342	$\sim 119,400$	254	74.3	0.05	0.02
3	528	$\sim 146,100$	381	72.2	0.04	0.04
4	386	$\sim 145,300$	308	79.8	0.04	-0.04

NOTES–
[a] XDEEP2 field number
[b] Number of X-ray sources in the XDEEP2 field
[c] Approximate number of optical sources in the XDEEP2 field region
[d] Number of X-ray sources with secure optical counterparts
[e] Percentage fraction of X-ray sources with secure optical counterparts
[f] Median positional offsets between the DEEP2 optical source co-ordinates and the X-ray source co-ordinates in arc-seconds

TABLE 7
DEEP2 X-RAY–OPTICAL COUNTERPART CATALOG

XDEEP2[a] Name	Field[b]	α_{J2000}[c] (^{o})	δ_{J2000}[c] (^{o})	DEEP2[d] Objno	α_{J2000}[e] (^{o})	δ_{J2000}[e] (^{o})	d_{OX}[f] (")	z[g]	P(gal)[h]	B	R	I
		X-ray			Optical					Photometry[i] (AB mag)		
aeg1_001	1	214.78246	52.99710	-	-	-	-	-	-	-	-	-
aeg1_002	1	214.78334	53.00712	13036677	214.78314	53.00728	0.72	0.5646	3	21.62	20.62	20.10
aeg1_003	1	214.79521	52.98033	13027633	214.79494	52.97998	1.38	0.7309	0.55	26.23	23.32	21.93
aeg1_004	1	214.79699	53.05600	13036612	214.79712	53.05598	0.29	-	3	20.31	18.55	17.91
aeg1_005	1	214.83506	53.04790	-	-	-	-	-	-	-	-	-
aeg1_006	1	214.83600	53.00792	13036601	214.83597	53.00809	0.63	-	-2	16.67	16.36	16.23
aeg1_007	1	214.84506	53.02555	13035495	214.84502	53.02559	0.20	-	3	24.37	24.62	23.94
aeg1_008	1	214.85376	52.99871	13027346	214.85321	52.99912	1.90	-	3	24.13	23.49	23.26
aeg1_009	1	214.85694	53.00549	13100779	214.85669	53.00582	1.28	-	3	24.69	24.47	24.27
aeg1_010	1	214.85765	53.01971	13035756	214.85777	53.02011	1.45	-	-2	22.79	21.16	20.41
aeg1_011	1	214.86239	53.03122	13035995	214.86253	53.03141	0.73	-	3	23.59	21.68	21.09
aeg1_012	1	214.86615	53.02515	-	-	-	-	-	-	-	-	-
aeg1_013	1	214.86670	52.97822	13027372	214.86674	52.97823	0.10	0.5608	0.81	23.00	22.87	22.61
aeg1_014	1	214.87337	53.03977	13035981	214.87335	53.03982	0.19	-	3	25.15	23.66	22.84
aeg1_015	1	214.87634	53.04383	13035650	214.87601	53.04362	1.03	0.3722	3	26.80	23.31	21.95
aeg1_016	1	214.87842	53.00748	13035444	214.87830	53.00769	0.81	-	1.00	26.06	23.14	22.27
aeg1_017	1	214.87886	52.98781	13027475	214.87888	52.98786	0.20	-	0.00	23.15	20.26	18.03
aeg1_018	1	214.88704	53.04167	-	-	-	-	-	-	-	-	-
aeg1_019	1	214.88706	52.99963	13027149	214.88704	52.99970	0.25	-	3	24.25	23.77	22.93
aeg1_020	1	214.88917	53.09005	-	-	-	-	-	-	-	-	-

NOTES–
[a] XDEEP2 unique source identifier
[b] XDEEP2 field number
[c] X-ray source position in J2000 co-ordinates (degrees)
[d] DEEP2 optical source identifier (Coil et al. 2004)
[e] Optical source position in J2000 co-ordinates (degrees)
[f] Angular separation between optical and X-ray source positions (arc-seconds)
[g] Redshift of optical counterpart
[h] Bayesian probability of being a galaxy based on R-band image (≤ 0: star/compact; ≥ 1: galaxy/extended; see Coil et al. 2004)
[i] Optical photometry in the B, R and I-bands (AB-magnitude)

sources in XDEEP2. When multiple optical counterparts are associated with one X-ray source, we accept the DEEP2 optical counterpart with the largest P_{match}. Given the cumulative distribution of P_{match} found for the XDEEP2 counterpart catalog, we expect a final spurious counterpart fraction of $\approx 4\%$. In Table 6 we show the breakdown by field of the number of X-ray sources with optical counterparts, the percentage identified and the median positional offset between the optical and X-ray source positions. We find that 943 ($\approx 75.1\%$) of the X-ray sources in Fields 2–4 have secure optical counterparts compared with 1183 ($\approx 68.8\%$) in Field 1. This higher fraction of secure counterparts in Fields 2–4 is, in all likelihood, due to the relatively shallow exposure of the *Chandra* observations in Fields 2–4 compared to those in Field 1, and hence, brighter X-ray sources tending towards bright optical host galaxies (i.e., X-ray-to-

optical flux ratios $\sim$ 1–10) which has been found previously in very shallow wide-field X-ray surveys (e.g., Maccacaro et al. 1988; Stocke et al. 1991; Akiyama et al. 2000; Lehmann et al. 2001; Murray et al. 2005). Indeed, AGN and QSOs are typically found to have similar ratios of $-1 < \log(f_X/f_O) < +1$ (e.g., Schmidt et al. 1998; Akiyama et al. 2000; Lehmann et al. 2001). In Figure 22 we show the full-band X-ray flux versus the DEEP2 R-band magnitude for the sources with secure optical counterparts. We illustrate approximate X-ray-to-optical flux ratios for the sources assuming the relation of McHardy et al. (2003), and we divide the sample between those optical sources identified in DEEP2 to be extended/galaxy ($P(\mathrm{gal}) > 0.3$; see Coil et al. 2004; Newman et al. 2012) and point-like sources (stellar or QSO; $P(\mathrm{gal}) < 0.3$). Of the 1559 optically extended X-ray-optical sources, $\approx 90\%$ (1425) have $\log(f_X/f_O) > -1$, suggesting a sig-
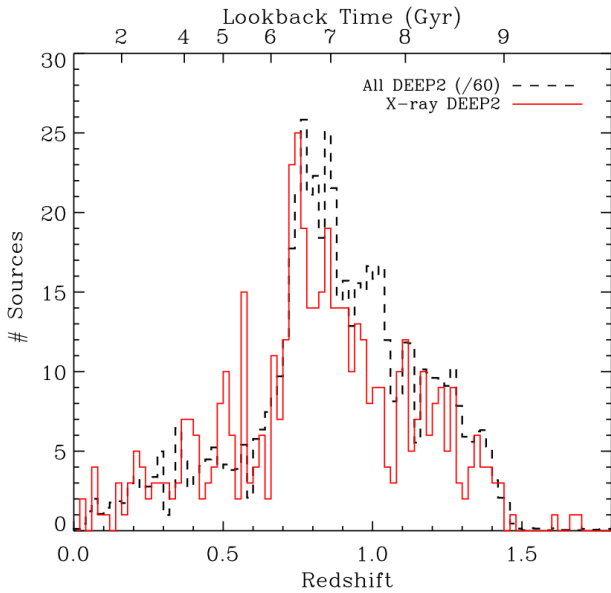
FIG. 23.— Redshift histograms for all 510 XDEEP2 galaxies with optical spectroscopic counterparts (solid-line) and all optical DEEP2 galaxies (dashed-line). The optical DEEP2 distribution is divided by a factor for 60 for ease of comparison to the X-ray sources. On the top-axis we show the present-day look-back times as a function of redshift, with $z = 0$ equivalent to $\tau_{lb} = 0$.

nificant fraction are bright AGN. We also find that 77 X-ray sources are also detected with very low X-ray-to-optical flux ratios (i.e., $\log(f_X/f_O) < -2$). These X-ray sources generally include normal galaxies, stars, and low-luminosity AGN, and as we show in Figure 22, all 77 X-ray–optical sources with $R_{\rm AB} < 18$ are point-like suggesting a stellar origin for the X-ray emission. As is clearly evident from the distribution of galaxies in Figure 22, our X-ray–optical source matching becomes incomplete towards optically-faint ($R \gtrsim 25$) systems for $f_X \lesssim 6 \times 10^{-15}\,{\rm erg\,cm^{-2}\,s^{-1}}$ due to the flux-limit of the optical DEEP2 data when compared to the depth of the X-ray observations within Field 1.

We also consider the $\approx 450,000$ optical galaxies identified in the CFHT Legacy Survey Deep 3 (CFHTLSD-3) field, which covers an area roughly coincident with the AEGIS 1–3 sub-fields and is complete to $i'_{\rm AB} < 27.0$ with sources detected down to $i'_{\rm AB} \sim 28.6$ (Ilbert et al. 2006; i.e., complete to ~ 2 magnitudes deeper than DEEP2). We find that 1009 X-ray sources have optical counterparts in the CFHTLSD-3 and 228/1009 were not previously identified in the DEEP2 catalog. Of the 228 X-ray sources, which were not previously identified to have optical DEEP2 counterparts, 163/228 have $i'_{\rm AB} > 24.4$ and 118 have $i'_{\rm AB} > 25.0$. With the subsequent inclusion of the CFHTLSD-3, we find an X-ray–optical counterpart fraction of $\approx 82\%$ within Field 1.

In Table 7 we provide the matching optical DEEP2 counterpart information for the entire XDEEP2 catalog (e.g., X-ray name; X-ray position; optical DEEP2 counterpart; positional offset; basic optical properties). Furthermore, to guide future multi-wavelength surveys, we additionally include the spectroscopic redshift information from the recently released DEEP2 DR4 catalog (Newman et al. 2012). Of the 2126 X-ray sources with optical counterparts, 700 are included as part of the spec-

troscopic catalog and 510/700 have secure extragalactic redshifts, with the majority in the range $0.3 \lesssim z \lesssim 1.4$ and the highest redshift source at $z \sim 3.04$. We show in Figure 23 that the X-ray sub-sample follows a similar redshift distribution to the main parent DEEP2 redshift catalog. Hence, in redshift terms, the X-ray sources may be considered a representative sample of the overall galaxy population in DEEP2. Future in-depth analyses of the AGN and galaxy redshift populations will allow us to understand the AGN clustering properties and possible correlations of AGN presence and large-scale structures.

6. SUMMARY

We have presented the X-ray source catalog and basic analyses of sources detected in the ≈ 10ks–1.1 Ms *Chandra* ACIS-I observations of the four X-ray DEEP2 (XDEEP2) survey fields. The total area of XDEEP2 is $\sim 3.2\,{\rm deg}^2$, and to date is the largest medium-deep *Chandra* X-ray survey constructed. Using wavelet decomposition software (`wvdecomp`), we detected X-ray point sources in the individual (non-merged) events and overlapping merged images in the 0.5–2 keV (soft-band [SB]), 2–7 keV (hard-band [HB]) and 0.5–7 keV (full-band [FB]) energy ranges, complete to a false-source probability threshold of 1×10^{-6}. When considering the survey regions where at least 10% of the area is sensitive, the flux limits in the merged observations are $f_{X,FB} > 2.8 \times 10^{-16}\,{\rm erg\,cm^{-2}\,s^{-1}}$, $f_{X,FB} > 4.5 \times 10^{-15}\,{\rm erg\,cm^{-2}\,s^{-1}}$, $f_{X,FB} > 4.6 \times 10^{-15}\,{\rm erg\,cm^{-2}\,s^{-1}}$ and $f_{X,FB} > 4.6 \times 10^{-15}\,{\rm erg\,cm^{-2}\,s^{-1}}$ in XDEEP2 Fields 1, 2, 3 and 4, respectively. The full XDEEP2 point source catalog contains 2976 sources, with 1720, 342, 528 and 386 sources in Fields 1–4. For the detected sources, we have presented the flux band ratio ($f_{\rm HB}/f_{\rm SB}$) distributions. Consistent with previous results, we confirm that low flux X-ray sources tend towards higher flux ratios ($f_{\rm HB}/f_{\rm SB} \sim 2$–10), consistent with that expected for flatter spectral slopes with $\Gamma \sim 1.2$–1.4.

We have performed a rigorous comparison between our new catalog of Field 1 and that previously presented in Laird et al. (2009). Our new catalog now contains the more recent 600 ks observations of three sub-fields within Field 1. We find excellent agreement between the two catalogs, and show that 96% of the sources identified in the previous catalog, using a substantially different detection technique, are also identified in the new catalog of Field 1. Through extensive source detection simulations, we suggest that the small $\approx 4\%$ discrepancy between the catalogs can be mainly attributed to our conservative removal of low-significance and possibly spurious sources. Indeed, with the inclusion of the low significance X-ray sources, we show that $\sim 99\%$ of the sources identified by Laird et al. would be identified here. Furthermore, we present a comparison between the *Chandra* Source Catalog (CSC) and the X-ray sources identified in the more shallow 10ks Fields 2, 3 and 4. We find that $\sim 41.9 \pm 2.2\%$ of the XDEEP2 sources within these fields are included in the CSC. The vast majority ($\approx 90\%$) of the XDEEP2 sources not identified in the CSC fall below their conservative detection threshold. We have presented the combined log N – log S distribution of soft-band detected sources identified across the XDEEP2 fields; the distribution shows

excellent agreement with the Extended *Chandra* Deep Field and *Chandra*-COSMOS fields to $f_{\rm X,0.5-2keV} \sim 2 \times 10^{-16}\,{\rm erg\,cm^{-2}\,s^{-1}}$. Given the large survey area of XDEEP2, we additionally place relatively strong constraints on the log N – log S distribution at high fluxes ($f_{\rm X,0.5-2keV} > 2 \times 10^{-14}\,{\rm erg\,cm^{-2}\,s^{-1}}$), and find a small systematic offset (a factor ~ 1.5) towards lower source numbers in the high-flux regime than observed previously in smaller area surveys. The number counts for sources with $f_{0.5-2keV} > 2 \times 10^{-14}\,{\rm erg\,cm^{-2}\,s^{-1}}$ are in close agreement with the X-ray background synthesis models of Gilli et al. (2007). However, based on our careful analyses of the uncertainty associated with the log N – log S distribution, derived through the use of a Monte-Carlo simulation, we find that at the 90% level we cannot reject the number count distribution predicted by the previous surveys.

We have additionally built upon a previous Bayesian-style method for associating the X-ray sources with their optical counterparts (Brand et al. 2006) in the DEEP2 photometric catalog (complete to $R_{\rm AB} < 25.2$; Coil et al. 2004), and find that 2126 of the X-ray sources presented here ($\approx 71.4 \pm 2.8\%$) have at least one secure optical counterpart. However, due to the much deeper X-ray exposure regions, we find a lower fraction of optical counterparts in Field 1 ($\approx 68.8\%$) compared with Fields 2–4 ($\approx 75.1\%$). We have additionally presented the optical photometric properties of the X-ray sources, the X-ray-to-optical ratios and find that the XDEEP2 sample have a similar redshift distribution to the main optical DEEP2 parent catalog, in the range $0 < z < 3$.

REFERENCES

Akiyama, M., Ohta, K., Yamada, T., et al. 2000, ApJ, 532, 700
Alexander, D. M., Brandt, W. N., Hornschemeier, A. E., et al. 2001, AJ, 122, 2156
Alexander, D. M., Bauer, F. E., Brandt, W. N., et al. 2003a, AJ, 126, 539
—. 2003b, AJ, 125, 383
—. 2011, ApJ, 738, 44
Alonso-Herrero, A., Pérez-González, P. G., Alexander, D. M., et al. 2006, ApJ, 640, 167
Barger, A. J., Cowie, L. L., Mushotzky, R. F., et al. 2005, AJ, 129, 578
Bauer, A. E., Grützbauch, R., Jørgensen, I., Varela, J., & Bergmann, M. 2011, MNRAS, 411, 2009
Bauer, F. E., Alexander, D. M., Brandt, W. N., et al. 2002, AJ, 123, 1163
Bell, E. F., Wolf, C., Meisenheimer, K., et al. 2004, ApJ, 608, 752
Boyle, B. J., & Terlevich, R. J. 1998, MNRAS, 293, L49
Brand, K., Dey, A., Brown, M. J. I., et al. 2005, ApJ, 626, 723
Brand, K., Brown, M. J. I., Dey, A., et al. 2006, ApJ, 641, 140
Brandt, W. N., & Hasinger, G. 2005, ARA&A, 43, 827
Brusa, M., Civano, F., Comastri, A., et al. 2010, ApJ, 716, 348
Cappelluti, N., Ajello, M., Burlon, D., et al. 2010, ApJ, 716, L209
Civano, F., Elvis, M., Brusa, M., et al. 2012, ArXiv 1205.5030
Coil, A. L., Newman, J. A., Kaiser, N., et al. 2004, ApJ, 617, 765
Coil, A. L., Georgakakis, A., Newman, J. A., et al. 2009, ApJ, 701, 1484
Cooper, M. C., Newman, J. A., Madgwick, D. S., et al. 2005, ApJ, 634, 833
Cooper, M. C., Newman, J. A., Croton, D. J., et al. 2006, MNRAS, 370, 198
Daddi, E., Alexander, D. M., Dickinson, M., et al. 2007, ApJ, 670, 173
Davis, M., Faber, S. M., Newman, J., et al. 2003, in Society of Photo-Optical Instrumentation Engineers (SPIE) Conference Series, Vol. 4834, Society of Photo-Optical Instrumentation Engineers (SPIE) Conference Series, ed. P. Guhathakurta, 161–172
Domínguez Sánchez, H., Pozzi, F., Gruppioni, C., et al. 2011, MNRAS, 417, 900
Done, C., Madejski, G. M., & Smith, D. A. 1996, ApJ, 463, L63+
Donley, J. L., Rieke, G. H., Pérez-González, P. G., Rigby, J. R., & Alonso-Herrero, A. 2007, ApJ, 660, 167
Ebeling, H., White, D. A., & Rangarajan, F. V. N. 2006, MNRAS, 368, 65
Elvis, M., Civano, F., Vignali, C., et al. 2009, ApJS, 184, 158
Evans, I. N., Primini, F. A., Glotfelty, K. J., et al. 2010, ApJS, 189, 37
Faber, S. M., Willmer, C. N. A., Wolf, C., et al. 2007, ApJ, 665, 265
Fassbender, R., Nastasi, A., Böhringer, H., et al. 2011, A&A, 527, L10+
Fiore, F., Puccetti, S., Brusa, M., et al. 2009, ApJ, 693, 447

Franceschini, A., Hasinger, G., Miyaji, T., & Malquori, D. 1999, MNRAS, 310, L5
Fukazawa, Y., Iyomoto, N., Kubota, A., Matsumoto, Y., & Makishima, K. 2001, A&A, 374, 73
Gehrels, N. 1986, ApJ, 303, 336
Georgakakis, A., Nandra, K., Laird, E. S., Aird, J., & Trichas, M. 2008, MNRAS, 388, 1205
Georgantopoulos, I., Akylas, A., Georgakakis, A., & Rowan-Robinson, M. 2009, A&A, 507, 747
Georgantopoulos, I., Rovilos, E., Xilouris, E. M., Comastri, A., & Akylas, A. 2011, A&A, 526, A86+
Giacconi, R., Zirm, A., Wang, J., et al. 2002, ApJS, 139, 369
Gilli, R., Comastri, A., & Hasinger, G. 2007, A&A, 463, 79
Gilli, R., Zamorani, G., Miyaji, T., et al. 2009, A&A, 494, 33
Goulding, A. D., Alexander, D. M., Mullaney, J. R., et al. 2011, MNRAS, 411, 1231
Hasinger, G., Burg, R., Giacconi, R., et al. 1993, A&A, 275, 1
Hasinger, G., Cappelluti, N., Brunner, H., Brusa, M., & et al. 2007, ApJS, 172, 29
Hasinger, G., Miyaji, T., & Schmidt, M. 2005, A&A, 441, 417
Hickox, R. C., & Markevitch, M. 2006, ApJ, 645, 95
Hickox, R. C., Jones, C., Forman, W. R., et al. 2009, ApJ, 696, 891
Hilton, M., Stanford, S. A., Stott, J. P., et al. 2009, ApJ, 697, 436
Hopkins, P. F., Hernquist, L., Cox, T. J., et al. 2006, ApJS, 163, 1
Hopkins, P. F., Hernquist, L., Cox, T. J., & Kereš, D. 2008, ApJS, 175, 356
Hopkins, P. F., Richards, G. T., & Hernquist, L. 2007, ApJ, 654, 731
Ilbert, O., Arnouts, S., McCracken, H. J., et al. 2006, A&A, 457, 841
Kenter, A., Murray, S. S., Forman, W. R., et al. 2005, ApJS, 161, 9
La Franca, F., Fiore, F., Comastri, A., et al. 2005, ApJ, 635, 864
Laird, E. S., Nandra, K., Georgakakis, A., et al. 2009, ApJS, 180, 102
Lehmann, I., Hasinger, G., Schmidt, M., et al. 2001, A&A, 371, 833
Lehmer, B. D., Brandt, W. N., Alexander, D. M., et al. 2005, ApJS, 161, 21
Lidman, C., Rosati, P., Tanaka, M., et al. 2008, A&A, 489, 981
Lira, P., Ward, M., Zezas, A., Alonso-Herrero, A., & Ueno, S. 2002, MNRAS, 330, 259
Luo, B., Bauer, F. E., Brandt, W. N., et al. 2008, ApJS, 179, 19
Maccacaro, T., Gioia, I. M., Wolter, A., Zamorani, G., & Stocke, J. T. 1988, ApJ, 326, 680
Madgwick, D. S., Coil, A. L., Conselice, C. J., et al. 2003, ApJ, 599, 997
Maiolino, R., Salvati, M., Bassani, L., et al. 1998, A&A, 338, 781
Matt, G., Brandt, W. N., & Fabian, A. C. 1996, MNRAS, 280, 823
McHardy, I. M., Gunn, K. F., Newsam, A. M., et al. 2003, MNRAS, 342, 802

Mehrtens, N., Romer, A. K., Hilton, M., et al. 2012, MNRAS, 2912

Meléndez, M., Kraemer, S. B., Schmitt, H. R., et al. 2008, ApJ, 689, 95

Moran, E. C., Lehnert, M. D., & Helfand, D. J. 1999, ApJ, 526, 649

Murray, S. S., Kenter, A., Forman, W. R., et al. 2005, ApJS, 161, 1

Nandra, K., Laird, E. S., Adelberger, K., et al. 2005, MNRAS, 356, 568

Nastasi, A., Fassbender, R., Böhringer, H., et al. 2011, A&A, 532, L6+

Newman, J. A., Cooper, M. C., Davis, M., et al. 2012, ArXiv 1203.3192

Papovich, C., Momcheva, I., Willmer, C. N. A., et al. 2010, ApJ, 716, 1503

Park, T., Kashyap, V. L., Siemiginowska, A., et al. 2006, ApJ, 652, 610

Puccetti, S., Vignali, C., Cappelluti, N., et al. 2009, ApJS, 185, 586

Richards, G. T., Strauss, M. A., Fan, X., et al. 2006, AJ, 131, 2766

Risaliti, G., Maiolino, R., & Salvati, M. 1999, ApJ, 522, 157

Schmidt, M., Hasinger, G., Gunn, J., et al. 1998, A&A, 329, 495

Serjeant, S., Bertoldi, F., Blain, A. W., Clements, D. L., & et al. 2010, A&A, 518, L7+

Silverman, J. D., Lamareille, F., Maier, C., et al. 2009, ApJ, 696, 396

Smolčić, V., Zamorani, G., Schinnerer, E., et al. 2009, ApJ, 696, 24

Stark, A. A., Gammie, C. F., Wilson, R. W., et al. 1992, ApJS, 79, 77

Stocke, J. T., Morris, S. L., Gioia, I. M., et al. 1991, ApJS, 76, 813

Tozzi, P., Gilli, R., Mainieri, V., et al. 2006, A&A, 451, 457

Ueda, Y., Akiyama, M., Ohta, K., & Miyaji, T. 2003, ApJ, 598, 886

Vikhlinin, A., Forman, W., Jones, C., & Murray, S. 1995, ApJ, 451, 564

Vikhlinin, A., McNamara, B. R., Forman, W., et al. 1998, ApJ, 502, 558

Willmer, C. N. A., Faber, S. M., Koo, D. C., et al. 2006, ApJ, 647, 853

Worsley, M. A., Fabian, A. C., Bauer, F. E., et al. 2005, MNRAS, 357, 1281

Xue, Y. Q., Luo, B., Brandt, W. N., et al. 2011, ApJS, 195, 10

Zheng, X. Z., Bell, E. F., Somerville, R. S., et al. 2009, ApJ, 707, 1566